Understanding single-phase water-management signatures in fuel-cell impedance spectra: A numerical study*

A. Kosakian[a,b], L. Padilla Urbina[a,c], A. Heaman[a], M. Secanell[a,*]

[a] *Energy Systems Design Laboratory, Department of Mechanical Engineering, University of Alberta, Canada*
[b] *Department of Mathematical and Statistical Sciences, University of Alberta, Canada*
[c] *Department of Chemical Engineering, University of Alberta, Canada*

Abstract

Electrochemical impedance spectroscopy is a powerful technique used in fuel-cell diagnosis and characterization. A low-frequency inductive behavior may appear in the fuel-cell-impedance spectrum and is believed to be related to the electrolyte-hydration dynamics. Since water management plays a crucial role in achieving high performance, understanding the electrolyte-hydration-related signatures of the impedance spectrum may help better interpret experimental data and design future fuel cells. In this work, an open-source, transient, single-phase 2D model is presented that is suitable for analyzing impedance spectra of proton-exchange-membrane fuel cells. Special care is taken to compare the model to transient polarization, ohmic-resistance, and impedance data measured in-house. The model reveals that the low-frequency inductive phenomenon is related to the finite-rate exchange of water between the electrolyte and the pores. Two inductive phenomena are observed, at 0.1–200 mHz and at 0.2–5 Hz, that are attributed to the water-transport dynamics in the electrolyte phase of the catalyst-coated membrane and in the catalyst layers, respectively. This work also shows an ohmic-resistance breakdown study that demonstrates that the high-frequency resistance is comprised of the ohmic resistance of the membrane and the electronically conductive components of the cell, but does not include protonic resistance of the carbon-supported catalyst layers.

Keywords: polymer electrolyte membrane fuel cell, proton exchange membrane fuel cell, electrochemical impedance spectroscopy, inductive behavior, electrolyte hydration

Nomenclature

$\Delta\overline{S}_{\text{overall}}$ entropy change per mole of hydrogen, J/(mol K)

$\boldsymbol{N}$ molar flux, mol/(cm^2 s)

$\boldsymbol{n}$ normal unit vector

$\overline{H}$ molar enthalpy, J/mol

*This is the authors' preprint of the article published in Electrochimica Acta on April 24, 2020 (`https://doi.org/10.1016/j.electacta.2020.136204`). This document does not contain the corrections made during the review and proof processes. Please cite the published article.

*Corresponding author
Email address: `secanell@ualberta.ca` (M. Secanell)

$\overline{H}_{\mathrm{lv}}$ molar latent heat of water vaporization, J/mol

$\overline{H}_{\mathrm{sorption}}$ molar enthalpy change due to water absorption/desorption by the electrolyte, J/mol

EW equivalent weight of the electrolyte, $\mathrm{g/mol}_{\mathrm{SO}_3^-}$

C capacitance, $\mathrm{F/cm}^3$, or specific heat capacity, $\mathrm{J/(g\,K)}$

c concentration, $\mathrm{mol/cm}^3$

D diffusion coefficient, cm^2/s

D_{T} thermo-osmotic diffusion coefficient for water in the electrolyte, $\mathrm{g/(cm\,s\,K)}$

F Faraday constant, ≈96485 C/mol

f_{ORR} fraction of the overall entropy change due to oxygen-reduction reaction

j volumetric current density, $\mathrm{A/cm}^3$

k_λ rate of absorption/desorption of water by the electrolyte, 1/s

k_{H_2} rate constant for hydrogen dissolution into the electrolyte, m/s

k_{O_2} rate constant for oxygen dissolution into the electrolyte, m/s

M molar mass, g/mol

n_{d} electro-osmotic drag coefficient for water in the electrolyte, $\mathrm{mol}_{\mathrm{H_2O}}/\mathrm{mol}_{\mathrm{H^+}}$

T temperature, K

t time, s

x molar fraction

Greek letters

κ thermal conductivity, $\mathrm{W/(cm\,K)}$

λ absorbed-water content in the electrolyte, $\mathrm{mol}_{\mathrm{H_2O}}/\mathrm{mol}_{\mathrm{SO}_3^-}$

ϕ potential, V

ρ density, $\mathrm{g/cm}^3$

σ electrical conductivity, S/cm

ε volume fraction

ξ portion of water produced electrochemically at the catalyst-ionomer interface

Subscripts and superscripts

H_2	hydrogen
H_2O	water
N_2	nitrogen
O_2	oxygen
0	property at the given operating conditions
dl	double layer
eff	effective transport property
eq	equilibrium
l	liquid water
m	electrolyte phase
s	solid, electronically conductive phase
tot	total
v	void phase (pore)
w	water vapor

1. Introduction

Hydrogen-fueled proton-exchange-membrane fuel cells (PEMFCs) convert the chemical energy of the fuel into electricity with the only bi-products being water and heat. Fuel-cell stacks and systems already meet the U.S. Department of Energy (DoE) targets for power density, specific power, and cold start-up time[1,2]; however, their cost and durability do not achieve the DoE goals[1,2]. Since catalyst layers are the most expensive components of the large-volume-production fuel-cell stacks[1,2], reduction or elimination of the use of expensive catalysts, such as platinum, is necessary to meet the targets[3]. Catalyst-reduction can be achieved through a substantial increase of the cell performance via improved charge, mass, and heat transport.

A crucial strategy for improving fuel-cell performance is water management, which aims at striking a balance between keeping the electrolyte hydrated (to support its conductivity[4–6]) and avoiding cell flooding by product water. Depending on the operating conditions, dynamic electrolyte hydration and liquid-water accumulation may result in the appearance of hysteresis in the measured polarization curves[7–12] and ohmic resistance of the cell[8,10–13]. Since polarization and resistance curves are usually measured during either voltage or current sweeps, the dynamics of various processes occurring in a fuel cell overlap, which complicates the transient analysis of the measurements. Electrochemical impedance spectroscopy (EIS)[14–22] allows the separation of the physical processes of different time scales in the frequency domain and to investigate their relative importance in the overall dynamic behavior of the

system. The EIS technique has been actively used in the experimental literature to investigate, for instance, charge transfer[14,23,24], protonic resistance of the catalyst layers[15–17,24–26], and mass transport[14,22–24,27,28].

An interesting feature of the fuel-cell impedance spectra is the inductive behavior at high and low frequencies[18]. While the high-frequency inductance is associated with the cables used in the measurements, the nature of the low-frequency inductive loop of fuel-cell spectra remains under debate and is a subject of a number of investigations (see the review by Pivac and Barbir[18] dedicated solely to that topic). This loop, typically appearing at frequencies under 1 Hz, has been claimed to be affected by electrolyte hydration[18,29–31], intermediates of the oxygen-reduction reaction (ORR)[17,18,20,29], platinum oxide formation[20,29,31], and carbon monoxide poisoning[18]. Understanding the low-frequency inductive behavior of fuel cells is thus necessary for future cell diagnosis and design.

The most common technique for analyzing fuel-cell impedance is the use of equivalent circuits to fit the experimental spectra[14–19,23,25,26,32,33]. However, the fitted parameters are only valid in the neighborhood of the tested operating conditions and cell composition. Oversimplification of the underlying physics may also result in a questionable meaning of the circuit elements and misunderstanding of the physicochemical phenomena behind the local features of the impedance spectra.

In contrast to equivalent circuits, physical models can be used to generate the impedance spectra through a direct numerical simulation of the cell. Such models have a predictive capability, which is impossible to achieve with a fitted circuit. Due to their complexity, however, physical models have not received widespread interest. Only a few one-dimensional[24,29,34–36] and multi-dimensional[31,37–40] models were used to investigate fuel-cell impedance, three of which[29,31,39] analyzed the inductive behavior.

Setzler and Fuller[29] attributed the low-frequency inductance to platinum-oxide formation in the catalyst layers and water accumulation in the membrane. Their isothermal model was able to predict the inductive loop observed experimentally at a wide range of current densities; however, inclusion of heat generation partially or completely offset the inductive behavior. Bao and Bessler[30,39] showed that the inductive loop decreases under a counterflow operation and when a thin membrane is used. They attributed the inductive behavior to the water-distribution dynamics in the membrane. Futter et al.[31] demonstrated that the low-frequency inductance is caused mainly by the dynamics in the catalyst-layer protonic conductivity, as well as membrane conductivity and RH-dependent local oxygen transport resistance in the catalyst layers. Both groups attributed the inductive behavior to the dynamic distribution of water in the electrolyte, but no in-depth parametric study of the water-transport mechanisms was performed. Additionally, the finite-rate water uptake by the electrolyte was neglected[31,38–40].

Recently, Schiefer et al.[20] performed an experimental investigation of the fuel-cell inductance. They attempted to magnify the effect of hydration on the inductive loop by using a higher relative humidity (RH) in the cathode than in the anode, but observed a reduction of the loop. They concluded that water transport was not the main cause of the low-frequency inductive behavior as the latter was stronger when RH was low and equal in both compartments. However, their data also showed the inductive loop increase in size when RH was reduced in the anode. It appears, therefore, that water imbalance in the cell does have a direct effect on the inductive behavior.

In this work, the hydration nature of the inductive loop is investigated with an open-source, single-phase, transient 2D PEMFC model based on the non-isothermal steady-state model by Bhaiya et al.[41,42]. Two-phase transport phenomena are not considered in this work, and all studies are performed under relatively low humidity to elucidate

and isolate the electrolyte-hydration effects in the impedance spectra. Unlike other physical EIS models[31,38–40], the model presented in this work takes the finite-rate exchange between water in the pores and in the electrolyte into account. The performed parametric studies of the water-transport mechanisms shed light on the fuel-cell inductance and, for the first time in the literature, unveil its relation to the water absorption/desorption kinetics in the ionomer. The low-frequency inductive loop is shown to only appear with non-zero rates of absorption and desorption of water by the electrolyte and when the vapor diffusion is sufficiently slow to allow for the uptake process to occur. The RH-imbalance study of Schiefer et al.[20] was revisited with our model, and it was shown to correctly predict the trends in the strength of the inductive behavior. The ratio of the back-diffusive and osmotic fluxes of water in the membrane and catalyst layers is shown to have a direct effect on the size of the inductive loop and even be responsible for the transformation of that loop into an additional capacitive arc when back-diffusion is relatively weak.

The developed model was also used to dispel the ambiguity between the terms "ohmic resistance" and "high-frequency resistance" present in the fuel-cell literature[14,16,17,30,32,33,38]. The ohmic-heating-based approach for calculating the ohmic resistance of the membrane-electrode-assembly (MEA) components introduced recently by Secanell et al.[43] was utilized in this work to perform an ohmic-resistance breakdown. The results indicate that the high-frequency resistance (HFR) is comprised of the protonic resistance of the membrane and the electronic resistance of other MEA components, as suggested by some authors[16,17,32,44]. Since fuel-cell HFR does not include the protonic resistance of the catalyst layers, the terms "ohmic resistance" and "high-frequency resistance" should not be used interchangeably.

Special care was taken in the model validation. Due to the large number of model parameters, using only one type of experimental data, e.g., polarization curves, is not sufficient to validate the model. Therefore, the presented model was thoroughly validated through transient polarization curves and ohmic-heating-based resistance at various operating conditions, as well as through EIS. In contrast to other models[31,38–40], no parameters were fitted to the experimental impedance spectra, and all simulations were performed with a single set of parameters based on the independent in-house measurements, manufacturer data, and literature.

This publication is organized as follows. The mathematical model, input parameters, and solution approach are presented in Section 2. Information about the experimentally tested cell and the operating conditions is given in Section 3. Validation of the model and a set of parametric studies highlighting the role of the electrolyte-hydration dynamics in the fuel-cell impedance are shown in Section 4. The paper is then concluded with Section 5, which summarizes the main results.

2. Mathematical model

2.1. Assumptions

The mathematical model used in this work was built upon the steady-state, non-isothermal, single-phase PEMFC model developed by Bhaiya et al.[41,42]. The main simplifying assumptions of the model are listed below.

1. Gas mixtures were assumed to be dilute, isobaric, and ideal. Gas flow was assumed purely diffusive at the considered operating conditions based on the recent study by Zhou et al.[45].
2. The model is single-phase, i.e., liquid-water transport was neglected at the considered conditions.

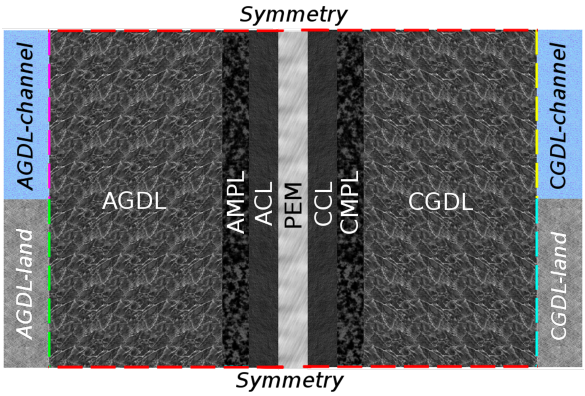

Figure 1: Computational domain of the model. Image not to scale.

3. Water transport in the electrolyte was assumed to take place in the absorbed form [41,42,45–49].
4. A single-energy-conservation-equation approach was used to describe heat transport under the assumption of local thermal equilibrium between the gas and solid phases due to sufficiently large interfacial area of the porous layers in the MEA [41,42].
5. The volumetric current density for ORR was computed with the double-trap kinetics model proposed by Wang et al. [50] and modified by Moore et al. [51]. The dual-path kinetics model [47,48,52] was used to compute the volumetric current density for the hydrogen oxidation reaction (HOR).
6. In order to account for the local reactant transport resistance in the catalyst layers (CLs), a uniform distribution of spherical ionomer-covered catalyst particles (ICCP) [43,53] was assumed in the CLs. In the ICCP model, the reactant gases (oxygen in the cathode and hydrogen in the anode) dissolve into and diffuse through a thin layer of ionomer before reaching the reaction sites.

Other assumptions are the same as in references [41,42,47,48]. The main assumptions specific to the transient processes are as follows.

1. Double-layer capacitance was assumed constant and uniformly distributed in the catalyst layers.
2. Kinetic models for ORR and HOR were assumed quasi-stationary. Transient terms describing dynamics of the reaction-intermediate concentrations were neglected.
3. The ICCP model was assumed quasi-stationary due to the small thickness of the ionomer film (2-10 nm), i.e., transient terms in the governing equations of this sub-model were neglected.

2.2. Governing equations

The model represents a two-dimensional, through-the-channel cross-section of a membrane-electrode assembly between parallel channels illustrated in Figure 1. The computational domain highlighted in dashed lines in Figure 1 contains a polymer electrolyte membrane sandwiched between two catalyst layers, two micro-porous layers, and two gas diffusion layers. Channels and bipolar-plate ribs are treated as boundary conditions.

Governing equations used in the model describe: a) transport of gases in the porous media of the MEA; b) electron transport in the gas-diffusion layers (GDLs), micro-porous layers (MPLs), and catalyst layers; c) proton transport in the proton-exchange membrane (PEM) and the electrolyte phase of the catalyst layers; d) transport of water

Table 1: Source terms in the PEMFC model.

Source term	GDL & MPL	CCL	ACL	PEM
$S_{\mathrm{O_2}}$	0	$-\frac{j}{4F}$	0	0
S_{w}	0	$(1-\xi)\frac{j}{2F} - \varepsilon_{\mathrm{m}} k_\lambda \frac{\rho_{\mathrm{m,\,dry}}}{\mathrm{EW}} (\lambda_{\mathrm{eq}} - \lambda)$	$-\varepsilon_{\mathrm{m}} k_\lambda \frac{\rho_{\mathrm{m,\,dry}}}{\mathrm{EW}} (\lambda_{\mathrm{eq}} - \lambda)$	0
$S_{\mathrm{H^+}}$	0	$-j$	j	0
$S_{\mathrm{e^-}}$	0	j	$-j$	0
S_λ	0	$\varepsilon_{\mathrm{m}} k_\lambda \frac{\rho_{\mathrm{m,\,dry}}}{\mathrm{EW}} (\lambda_{\mathrm{eq}} - \lambda) + \xi \frac{j}{2F}$	$\varepsilon_{\mathrm{m}} k_\lambda \frac{\rho_{\mathrm{m,\,dry}}}{\mathrm{EW}} (\lambda_{\mathrm{eq}} - \lambda)$	0
S_{T}	$\sigma_{\mathrm{s}}^{\mathrm{eff}} (\nabla\phi_{\mathrm{s}} \cdot \nabla\phi_{\mathrm{s}})$	$-j\eta + \frac{j}{2F}\left(-T f_{\mathrm{ORR}} \Delta\overline{S}_{\mathrm{overall}} - (1-\xi)\overline{H}_{\mathrm{lv}}\right) +$ $\sigma_{\mathrm{s}}^{\mathrm{eff}} (\nabla\phi_{\mathrm{s}} \cdot \nabla\phi_{\mathrm{s}}) +$ $\sigma_{\mathrm{m}}^{\mathrm{eff}} (\nabla\phi_{\mathrm{m}} \cdot \nabla\phi_{\mathrm{m}}) +$ $\varepsilon_{\mathrm{m}} k_\lambda \frac{\rho_{\mathrm{m,\,dry}}}{\mathrm{EW}} (\lambda_{\mathrm{eq}} - \lambda)\, \overline{H}_{\mathrm{sorption}}$	$j\eta + \frac{j}{2F}\left(-T\,(1 - f_{\mathrm{ORR}})\,\Delta\overline{S}_{\mathrm{overall}}\right) +$ $\sigma_{\mathrm{s}}^{\mathrm{eff}} (\nabla\phi_{\mathrm{s}} \cdot \nabla\phi_{\mathrm{s}}) +$ $\sigma_{\mathrm{m}}^{\mathrm{eff}} (\nabla\phi_{\mathrm{m}} \cdot \nabla\phi_{\mathrm{m}}) +$ $\varepsilon_{\mathrm{m}} k_\lambda \frac{\rho_{\mathrm{m,\,dry}}}{\mathrm{EW}} (\lambda_{\mathrm{eq}} - \lambda)\, \overline{H}_{\mathrm{sorption}}$	$\sigma_{\mathrm{m}}^{\mathrm{eff}} (\nabla\phi_{\mathrm{m}} \cdot \nabla\phi_{\mathrm{m}})$

absorbed in the PEM and the electrolyte phase of the CLs; and e) thermal transport in all MEA components. The governing equations are as follows:

$$\varepsilon_{\mathrm{v}} c_{\mathrm{tot}} \frac{\partial x_{\mathrm{O_2}}}{\partial t} - \nabla \cdot \left(c_{\mathrm{tot}} D_{\mathrm{O_2}}^{\mathrm{eff}} \nabla x_{\mathrm{O_2}}\right) = S_{\mathrm{O_2}}, \tag{1}$$

$$\varepsilon_{\mathrm{v}} c_{\mathrm{tot}} \frac{\partial x_{\mathrm{w}}}{\partial t} - \nabla \cdot \left(c_{\mathrm{tot}} D_{\mathrm{w}}^{\mathrm{eff}} \nabla x_{\mathrm{w}}\right) = S_{\mathrm{w}}, \tag{2}$$

$$-C_{\mathrm{dl}} \frac{\partial \eta}{\partial t} - \nabla \cdot \left(\sigma_{\mathrm{m}}^{\mathrm{eff}} \nabla \phi_{\mathrm{m}}\right) = S_{\mathrm{H^+}}, \tag{3}$$

$$C_{\mathrm{dl}} \frac{\partial \eta}{\partial t} - \nabla \cdot \left(\sigma_{\mathrm{s}}^{\mathrm{eff}} \nabla \phi_{\mathrm{s}}\right) = S_{\mathrm{e^-}}, \tag{4}$$

$$\varepsilon_{\mathrm{m}} \frac{\rho_{\mathrm{m,\,dry}}}{\mathrm{EW}} \frac{\partial \lambda}{\partial t} - \nabla \cdot \left(n_{\mathrm{d}} \frac{\sigma_{\mathrm{m}}^{\mathrm{eff}}}{F} \nabla \phi_{\mathrm{m}} + \frac{\rho_{\mathrm{m,\,dry}}}{\mathrm{EW}} D_\lambda^{\mathrm{eff}} \nabla \lambda + \frac{D_{\mathrm{T}}^{\mathrm{eff}}}{M_{\mathrm{H_2O}}} \nabla T\right) = S_\lambda, \tag{5}$$

$$\frac{\partial}{\partial t}\left(\sum_{i=\mathrm{phase}} \varepsilon_i \rho_i C_i T\right) - \nabla \cdot \left(\kappa^{\mathrm{eff}} \nabla T\right) + \sum_{j=\mathrm{gas},\,\lambda} \left(\boldsymbol{N}_j \cdot \nabla \overline{H}_j\right) = S_{\mathrm{T}}, \tag{6}$$

where $\eta = \phi_{\mathrm{s}} - \phi_{\mathrm{m}} - E_{\mathrm{th}}$ is the overpotential (V) and E_{th} is the theoretical half-cell potential for each reaction (V).

Mass-transport equations for nitrogen in the cathode and hydrogen in the anode are not solved and the respective molar fractions are obtained as $x_{\mathrm{N_2}} = 1 - x_{\mathrm{O_2}} - x_{\mathrm{w}}$ and $x_{\mathrm{H_2}} = 1 - x_{\mathrm{w}}$. Source terms of equations (1)-(6) are listed in Table 1. They account for the hydrogen-oxidation and oxygen-reduction reactions taking place in the anode and cathode catalyst layers, respectively, finite-rate exchange of water between the electrolyte and vapor, and heat sources and sinks. The latter include irreversible and reversible heat generation due to the half-cell reactions, heat sink due to the assumed complete vaporization of the liquid water produced in the ORR, ohmic heating, and heat generation and consumption due to absorption and desorption of water by the electrolyte in the catalyst layers. It is assumed that a portion of the product water is generated directly at the catalyst-electrolyte interface. This is approximated by moving a portion of the water production term, $\xi j_{\mathrm{f,e}}/(2F)$, where $\xi \in [0,\,1]$, from the source term in equation (2) to the source term of the absorbed-water transport equation (5) (hence the $(1-\xi)$ multiplier in the first term of equation (2) in Table 1).

Gas transport is only modeled in the porous layers (GDLs, MPLs, CLs), proton and absorbed-water transport

Table 2: Solution-variable domains in the PEMFC model.

Solution variable	AGDL, AMPL	ACL	PEM	CCL	CMPL, CGDL
x_{O_2}				✓	✓
x_w	✓	✓		✓	✓
ϕ_m		✓	✓	✓	
ϕ_s	✓	✓		✓	✓
λ		✓	✓	✓	
T	✓	✓	✓	✓	✓

Table 3: Boundary conditions in the PEMFC model.

Solution variable	AGDL-channel	AGDL-land	CGDL-channel	CGDL-land	Symmetry
x_{O_2}	no flux	no flux	$x_{O_2} = x^0_{O_2}$	no flux	no flux
x_w	$x_w = x^0_{w,a}$	no flux	$x_w = x^0_{w,c}$	no flux	no flux
ϕ_m	no flux	no flux	no flux	no flux	no flux
ϕ_s	no flux	$\phi_s = 0$	no flux	$\phi_s = V_{cell}(t)$	no flux
λ	no flux	no flux	no flux	no flux	no flux
T	no flux	$T = T_{a,land} = T^0$	no flux	$T = T_{c,land} = T^0$	no flux

is modeled in the electrolyte phase (CLs, PEM), and electron transport is modeled in the solid phase of the MEA (GDLs, MPLs, CLs). This is summarized in Table 2.

2.3. Initial and boundary conditions

The initial solution was pre-computed by solving equations (1)-(6) at steady state, i.e., with all transient terms set to zero. This solution was then imported into the transient model as an initial solution at the start of the voltage-sweep and impedance-spectroscopy simulations.

Boundary conditions are listed in Table 3, where $V_{cell}(t)$ is the time-dependent operating voltage and the values with the zero superscript are computed based on the operating conditions as discussed in reference [47]. Gaseous species were not allowed to leave the domain through the GDL-land interfaces; similarly, no charge was allowed to leave the MEA through the GDL-channel boundaries. This, along with the symmetry conditions, was described by the no-flux boundary conditions.

2.4. Microscale catalyst-layer model

Local reactant transport resistance in the catalyst layers was accounted for by incorporating an additional sub-model describing transport of reactants through the thin ionomer films covering spherical catalyst particles (the ICCP model [43,53]). This model is based on a mass balance between the reactant transport through the gas-ionomer interface, its diffusion through the ionomer film, and consumption at the catalyst surface.

The rate of oxygen entering the ICCP through the gas-ionomer interface (in mol/s) is given by [43,53]

$$R^{int}_{O_2} = -4\pi(r_{core} + \delta)^2 k_{O_2} \left(c_{O_2,g|f} - c^{eq}_{O_2,g|f} \right),$$

where r_{core} is the radius of the ICCP carbon-platinum core, δ is the thickness of the ionomer film in the ICCP computed from the known platinum and electrolyte loading of the catalyst layer[43,53], $c_{\text{O}_2,\text{g|f}}$ is the oxygen concentration in the ionomer at the gas-ionomer film interface, and $c^{\text{eq}}_{\text{O}_2,\text{g|f}}$ is its equilibrium value obtained from Henry's law at the given partial pressure of oxygen. The rate of oxygen diffusion through a spherical surface of area $4\pi r^2$ is given by[43,53]

$$R^{\text{diff}}_{\text{O}_2} = 4\pi r^2 D_{\text{O}_2,\text{m}} \frac{dc_{\text{O}_2}}{dr},$$

where $D_{\text{O}_2,\text{m}}$ is the diffusion coefficient of oxygen in the ionomer. Consumption of oxygen in the ORR at the catalyst surface is described by[43,53]

$$R^{\text{ORR}}_{\text{O}_2} = \frac{i(c_{\text{O}_2,\text{c|f}},\eta)A_{\text{s}}}{4F},$$

where $i(c_{\text{O}_2,\text{c|f}},\eta)$ is the current density computed based on the concentration of oxygen in the ionomer at the catalyst surface $c_{\text{O}_2,\text{c|f}}$. Here, A_{s} is the active surface area of the catalyst in one ICCP:

$$A_{\text{s}} = \frac{A_{\text{v}}}{1-\varepsilon_{\text{v}}} \frac{4}{3}\pi(r_{\text{core}}+\delta)^3,$$

where A_{v} is the experimentally measured active area per volume of the catalyst layer.

At steady state, $R^{\text{ORR}}_{\text{O}_2} = R^{\text{int}}_{\text{O}_2}$ and $R^{\text{ORR}}_{\text{O}_2} = R^{\text{diff}}_{\text{O}_2}$ form a system of equations for the unknown $c_{\text{O}_2,\text{g|f}}$ and $c_{\text{O}_2,\text{c|f}}$. Integrating the ODE $R^{\text{ORR}}_{\text{O}_2} = R^{\text{diff}}_{\text{O}_2}$ from r_{core} to $r_{\text{core}}+\delta$ and eliminating $c_{\text{O}_2,\text{g|f}}$, the following equation is obtained[43,53]:

$$c_{\text{O}_2,\text{c|f}} = c^{\text{eq}}_{\text{O}_2,\text{g|f}} - \frac{i(c_{\text{O}_2,\text{c|f}},\eta)A_{\text{s}}}{16F\pi}\left(\frac{1}{(r_{\text{core}}+\delta)^2 k_{\text{O}_2}} + \frac{\delta}{r_{\text{core}}(r_{\text{core}}+\delta)D_{\text{O}_2,\text{m}}}\right). \tag{7}$$

Equation (7) is implicit in $c_{\text{O}_2,\text{c|f}}$ and is solved using Newton's method (the solution is accepted once the residual of equation (7) reaches 10^{-12}). The ICCP model allows the correction of the local current density with respect to the local oxygen transport resistance in the cathode catalyst layer. The volumetric current density in the catalyst layer used in the source terms of the PEMFC model (Table 1) is computed as $j = i(c_{\text{O}_2,\text{c|f}},\eta)A_{\text{v}}$. Similar equations apply for the anode side. This model is quasi-stationary and depends on time through gas concentration and overpotential.

2.5. Input parameters

The main input parameters and the relations used to compute the various material and transport properties are listed in Tables 4–8. The rest of the parameters and relations are given in the Supplementary Information and in references[41,42,47,48]. The majority of the model parameters came from the literature, independent in-house measurements, and the manufacturer data. The unknown parameters were modified in this work to calibrate the model so that the predicted data were in agreement with the experiments. Those parameters are discussed next with a special attention to the hydration-related parameters that play a central role in the ability of the model to accurately predict the electrolyte-hydration dynamics and ohmic resistance of the cell.

Table 4: Operating conditions and geometrical parameters.

Parameter	**Value**	**Details**
	Operating conditions	

Table 4: (Continued) Operating conditions and geometrical parameters of the cell.

Parameter	Value	Details
Temperature, K	353.15	
Pressure, atm	1.5	50 kPa backpressure
RH	0.3, 0.5, or 0.7	
Cell geometry		
Land width, μm	827	Measured (optical microscope)
Channel width, μm	819	Measured (optical microscope)
MEA area, cm^2	5	Controlled (inkjet printing)

Table 5: Model parameters for the catalyst layers.

Parameter	Value/expression	Details
Geometry and structure		
Thickness, μm	2.8 (anode), 4.5 (cathode)	Measured (SEM)
Porosity	$\varepsilon_v = 0.47$ (anode), $\varepsilon_v = 0.53$ (cathode)	Computed[a]
Solid-phase volume fraction	$\varepsilon_s = 0.34$ (anode), $\varepsilon_s = 0.30$ (cathode)	Computed[a]
Ionomer-phase volume fraction	$\varepsilon_m = 0.19$ (anode), $\varepsilon_m = 0.17$ (cathode)	Computed[a]
Primary-particle radius, nm	$r_p = 39.5$	Manufacturer [54]
Gas transport		
Gas diffusivity	$\frac{1}{D} = \frac{1}{D_{mol}} + \frac{1}{D_K}$	Ref. [55]
Molecular diffusivity of gases	Chapman-Enskog theory	Refs. [55,56]
Knudsen diffusivity	$D_K = \frac{2r_K}{3}\sqrt{\frac{8RT}{\pi M}}$	Ref. [55]
Knudsen pore radius	$r_K = r_p\left(1.66\varepsilon_v^{1.65} + 0.289\right)$	Refs. [57,58]
Effective gas diffusivity	$D^{eff} = \begin{cases} D\left(\frac{\varepsilon_v - 0.05}{0.95}\right)^{1.9}, & \varepsilon_v \geq 0.05 \\ 0, & 0 < \varepsilon_v < 0.05 \end{cases}$	Refs. [57,58]
Electrolyte hydration and absorbed-water transport		
Sorption isotherm, $mol_{H_2O}/mol_{SO_3^-}$	$\lambda_{eq} = \begin{cases} \left[6.932a_w - 14.53a_w^2 + 11.82a_w^3\right] \cdot \exp\left(-2509\left(\frac{1}{T} - \frac{1}{303.15}\right)\right), & 0 < a_w < 1 \\ 22, & a_w \geq 1 \end{cases}$	This work[b]
Back-diffusion coefficient for absorbed water, cm^2/s	$D_\lambda = 5.44 \cdot 10^{-5} f_V \frac{\partial \ln a_w}{\partial \ln \lambda_{eq}} \exp\left[\frac{20000}{R}\left(\frac{1}{303} - \frac{1}{T}\right)\right]$, where $f_V = \frac{\lambda V_w}{V_e + \lambda V_w}$, $V_w = \frac{M_{H_2O}}{\rho_l}$, $V_e = \frac{EW}{\rho_{m,\,dry}}$	Refs. [59,60], this work[b]
Darken factor	$\frac{\partial \ln a_w}{\partial \ln \lambda_{eq}} = \begin{cases} \exp\left(0.7647\lambda_{eq,\,corr}^{2.305}\right), & \lambda_{eq,\,corr} < 1.209 \\ 3.266 + 2.930\Big[\exp\Big(-6.735 \cdot (\lambda_{eq,\,corr} - 1.209)\lambda_{eq,\,corr}^{-0.8994}\Big) - 1\Big], & \lambda_{eq,\,corr} \geq 1.209 \end{cases}$ where $\lambda_{eq,\,corr} = \lambda_{eq}\exp\left(2509\left(\frac{1}{T} - \frac{1}{303.15}\right)\right)$	Computed from the sorption isotherm[b]
Electro-osmotic drag coefficient for absorbed water, mol_{H_2O}/mol_{H^+}	$n_d = \frac{2.5\lambda}{22}$	Ref. [46]

Table 5: (Continued) Model parameters for the catalyst layers.

Parameter	Value/expression	Details
Diffusion coefficient for the thermal osmosis of absorbed water, g/(cm s K)	$D_{\mathrm{T}} = -1.04 \cdot 10^{-4} \exp\left(-\frac{2362}{T}\right)$	Ref. [61]
Rate of water absorption/desorption by the electrolyte, 1/s	$k_\lambda = \frac{\alpha}{L_{\mathrm{CL}}} f_{\mathrm{V}} \exp\left[\frac{20000}{R}\left(\frac{1}{303} - \frac{1}{T}\right)\right]$ where $\alpha = \begin{cases} 4.59 \cdot 10^{-5} \text{ cm/s}, & \lambda < \lambda_{\mathrm{eq}}, \\ 41.31 \cdot 10^{-5} \text{ cm/s}, & \lambda > \lambda_{\mathrm{eq}} \end{cases}$	Ref. [59], this work[b]
Portion of ORR water produced in the electrolyte phase	$\xi = 0.03$	This work[c]
Charge transfer		
Proton conductivity, S/cm	$\sigma_{\mathrm{m}} = \left(-8 \cdot 10^{-3} + 7.5 \cdot 10^{-4}\omega - 6.375 \cdot 10^{-6}\omega^2 + 1.93 \cdot 10^{-7}\omega^3\right) \exp\left[\frac{6248}{R}\left(\frac{1}{353} - \frac{1}{T}\right)\right]$, where $\omega = \begin{cases} 100\left(-0.1254 + 0.1832\lambda - 0.00865\lambda^2 + 0.000094\lambda^3\right), & 0 < \lambda < 13 \\ 100, & \lambda \geq 13 \end{cases}$	Refs. [62]
Effective transport properties in the electrolyte phase	$Q^{\mathrm{eff}} = \varepsilon_{\mathrm{m}}^{1.6} Q$	Refs. [41,42,62]
Electron conductivity, S/cm	$\sigma_{\mathrm{s}} = 88.84$	Refs. [41,47,48]
Effective electron conductivity	$\sigma_{\mathrm{s}}^{\mathrm{eff}} = \begin{cases} \sigma_{\mathrm{s}}\left(\frac{\varepsilon_{\mathrm{s}} - 0.12}{0.88}\right)^2, & \varepsilon_{\mathrm{s}} \geq 0.12 \\ 0, & 0 < \varepsilon_{\mathrm{s}} < 0.12 \end{cases}$	Ref. [47]
Volumetric double-layer capacitance, F/cm^3	54	Measured (cyclic voltammetry)
Thermal transfer		
Effective thermal conductivity, mW/(cm K)	2.7[d]	Ref. [63]
ICCP sub-model parameters		
ICCP film thickness, nm	6.4	Computed[a]
ICCP oxygen-dissolution rate constant, m/s	$k_{\mathrm{O_2}} = 4.7 \cdot 10^{-4}$	This work[e]
ICCP hydrogen-dissolution rate constant, m/s	$k_{\mathrm{H_2}} = 10^{-1}$	Ref. [43]

[a] Computed from catalyst and ionomer loading.

[b] Adopted from the cited literature and modified for the simulated dynamic HFR response to match the in-house experimental data. See the details in the text.

[c] Estimated based on the simulated and experimental HFR dynamics. See the details in the text.

[d] Assumed constant value measured by Khandelwal and Mench [63] and within the range reported by Burheim et al. [64].

[e] Estimated based on the simulated and experimental limiting current density with 1% oxygen. See the details in the text.

Table 6: Model parameters for the Nafion® NR-211 membrane.

Parameter	Value/expression	Details
Thickness, μm	25	Manufacturer

Table 6: (Continued) Model parameters for the Nafion® NR-211 membrane.

Parameter	Value/expression	Details
Back-diffusion coefficient for absorbed water, cm^2/s	$D_\lambda = 3.2 \cdot \begin{cases} 3.10 \cdot 10^{-3}\lambda\,(\exp(0.28\lambda)-1)\exp\left[-\frac{2436}{T}\right], & 0<\lambda\leq 3 \\ 4.17 \cdot 10^{-4}\lambda\,(161\exp(-\lambda)+1)\exp\left[-\frac{2436}{T}\right], & \lambda>3 \end{cases}$	Ref. [65], this work[a]
Electro-osmotic drag coefficient for absorbed water, mol_{H_2O}/mol_{H^+}	$n_d = \frac{2.5\lambda}{22}$	Ref. [46]
Diffusion coefficient for the thermal osmosis of absorbed water, g/(cm s K)	$D_T = -1.04 \cdot 10^{-4}\exp\left(-\frac{2362}{T}\right)$	Ref. [61]
Proton conductivity, S/cm	$\sigma_m = \left(0.020634 + 0.01052\lambda - 1.0125 \cdot 10^{-4}\lambda^2\right) \cdot \exp\left[\frac{6248}{R}\left(\frac{1}{303}-\frac{1}{T}\right)\right]$	Refs. [66,67]
Thermal conductivity, mW/(cm K)	1.5[b]	Refs. [63,68]

[a] Adopted from the cited literature and modified for the simulated dynamic HFR response to match the in-house experimental data. See the details in the text.

[b] Assumed constant value within the range reported for the dry Nafion® by Khandelwal and Mench [63] and for the hydrated Nafion® by Burheim et al. [68].

Table 7: Model parameters for the gas-diffusion layers (SGL 29BC).

Parameter	Value/expression	Details
Thickness, μm	192 (uncompressed), 109 (compressed)[a]	Manufacturer [69], ref. [70], this work
Porosity	0.89 (uncompressed), 0.81 (compressed)[a]	Manufacturer [69], ref. [70], this work
Molecular diffusivity of gases	Chapman-Enskog theory	Refs. [55,56]
Effective gas diffusivity (in-plane)[b]	$D^{\text{eff}} = \begin{cases} D\left(\frac{\varepsilon_v - 0.12}{0.88}\right)^2, & \varepsilon_v \geq 0.12 \\ 0, & 0 < \varepsilon_v < 0.12 \end{cases}$	Refs. [57,71]
Effective gas diffusivity (through-plane)[b]	$D^{\text{eff}} = \begin{cases} D\left(\frac{\varepsilon_v - 0.12}{0.88}\right)^{4.9}, & \varepsilon_v \geq 0.12 \\ 0, & 0 < \varepsilon_v < 0.12 \end{cases}$	Refs. [57,71]
Effective electron conductivity (in-plane), S/cm	180[c]	Manufacturer [69]
Effective electron conductivity (through-plane), S/cm	3.75[c]	Manufacturer [69]
Effective thermal conductivity (in-plane), W/(m K)[d]	$\kappa_{ip}^{\text{eff}} = -7.166 \cdot 10^{-6}T_C^3 + 2.24 \cdot 10^{-3}T_C^2 - 0.237T_C + 20.1$, where $T_C = T - 273.15$	Refs. [41,42]
Effective thermal conductivity (through-plane), W/(m K)[d]	$\kappa_{tp}^{\text{eff}} = M(T_C)\kappa_{ip}^{\text{eff}}$, where $M(T_C) = -1.495 \cdot 10^{-11}T_C^5 + 2.601 \cdot 10^{-9}T_C^4 - 6.116 \cdot 10^{-8}T_C^3 - 9.829 \cdot 10^{-6}T_C^2 + 8.754 \cdot 10^{-4}T_C + 0.0664$	Refs. [41,42]

[a] Computed compressed values based on the SGL 29AA GDL data from the manufacturer [69] using the approach discussed in the Supplementary Information

[b] Taken to match the in-plane diffusibility D^{eff}/D of SGL 29BA GDL measured by Xu [71] and to account for the fact that the through-plane diffusibility of GDLs is typically half of that in the in-plane direction [57,72].

[c] At 1 MPa of compression [69].

[d] Fitted by Bhaiya et al. [41,42] to the experimental data for Toray® TGP-H-120 GDLs [73,74]. The produced thermal conductivity is similar to that computed for the compressed SGL 29AA GDLs based on the manufacturer's data [69] (see Supplementary Information).

Table 8: Model parameters for the micro-porous layers (SGL 29BC).

Parameter	**Value/expression**	**Details**
Thickness, μm	37	Ref. [70]
Porosity	0.58	Measured (MIP)[a]
Gas diffusivity	$\frac{1}{D} = \frac{1}{D_{\text{mol}}} + \frac{1}{D_{\text{K}}}$	Ref. [55]
Molecular diffusivity of gases	Chapman-Enskog theory	Refs. [55,56]
Knudsen diffusivity	$D_{\text{K}} = \frac{2r_{\text{K}}}{3}\sqrt{\frac{8RT}{\pi M}}$	Ref. [55]
Knudsen pore radius, nm	56	Measured (MIP)[a]
Effective gas diffusivity	$D^{\text{eff}} = \begin{cases} D\left(\frac{\varepsilon_{\text{v}}-0.05}{0.95}\right)^{1.9}, & \varepsilon_{\text{v}} \geq 0.05 \\ 0, & 0 < \varepsilon_{\text{v}} < 0.05 \end{cases}$	Refs. [57,58[b]]
Effective electron conductivity (in-plane), S/cm	121[c]	Manufacturer [69], this work
Effective electron conductivity (through-plane), S/cm	0.95[c]	Manufacturer [69], this work
Effective thermal conductivity (in-plane), W/(m K)	$4.5\left(0.31\varepsilon_{\text{v}}^2 - 0.6\varepsilon_{\text{v}} + 0.36\right)$	This work[d]
Effective thermal conductivity (through-plane), W/(m K)	$4.5\left(-0.22\varepsilon_{\text{v}}^2 + 0.22\varepsilon_{\text{v}} - 0.01\right)$	This work[d]

[a] Based on the raw mercury-intrusion porosimetry (MIP) data from another publication from our laboratory [70]. Pore-size distribution (PSD) of the MPL was found by subtracting the PSD of SGL 29BA GDL samples from SGL 29BC GDL-MPL samples.

[b] Assumed same expression as in the stochastically reconstructed catalyst layers [57,58] due to similar microstructure.

[c] Computed compressed values based on the SGL 29AA GDL and SGL 29BC GDL-MPL data from the manufacturer [69]. See the approach in the Supplementary Information. The artificial anisotropy of the MPL may be attributed to the composite sub-layer that exists at the GDL-MPL interface [75,76], which is affected by the alignment of the GDL fibers in that region.

[d] Fitted in this work with $R^2 \geq 0.989$ to the thermal conductivity of the stochastically reconstructed MPLs reported by Zamel et al. [77]. Valid for $\varepsilon_{\text{v}} \in (0.47, 0.78)$.

2.5.1. Water uptake by the electrolyte in the catalyst layers

Mathematical models of PEMFCs available in the literature primarily use sorption isotherms measured for the electrolyte membranes (see, for instance, [11,13,31,39,42,45,49,78–84]). Those isotherms often do not contain temperature correction [11,78–84], which may limit their applicability at different operating temperature and in non-isothermal applications. Moreover, a number of studies [85–91] suggested that the water uptake in the catalyst layers and ultrathin Nafion® films is suppressed compared to bulky membranes at the same temperature and RH conditions. Water uptake similar to that in the membranes was also observed [4,90–93].

The experimental uptake data for catalyst layers and pseudo catalyst layers [4,85,89] were fitted in this work in order to obtain a relation for computing the equilibrium water content λ_{eq} in the electrolyte phase of the fuel-cell catalyst

layers. The final water-uptake relation had R^2 of at least 0.990 and is given in Table 5.

The detailed information about the fitting process and the plot of the experimental data and the fitted uptake curves are given in the Supplementary Information The sorption isotherm shown in Table 5 can be used to model vapor-equilibrated water uptake in the catalyst layers of fuel cells at 25–80 °C and produces reasonable sorption isotherms (in terms of the shape of the curve) at the temperature values up to 120 °C.

2.5.2. Absorbed-water diffusivity in the electrolyte

Catalyst layers. The diffusion coefficient for water absorbed into the electrolyte of the catalyst layers was computed through the Darken factor and the diffusion coefficient of water related to the chemical-potential gradient [59,60,65,94]

$$D_\lambda = \underbrace{\frac{\partial \ln a_\mathrm{w}}{\partial \ln \lambda_\mathrm{eq}}}_{\text{Darken factor}} D_\mu,$$

where

$$D_\mu = \alpha_\lambda f_\mathrm{V} \exp\left[\frac{20000}{R}\left(\frac{1}{303} - \frac{1}{T}\right)\right], \tag{8}$$

α_λ (cm^2/s) is a constant prefactor treated as a fitting parameter,

$$f_\mathrm{V} = \frac{\lambda V_\mathrm{w}}{V_\mathrm{e} + \lambda V_\mathrm{w}}, \tag{9}$$

is the volume fraction of water in the electrolyte, V_w is the molar volume of water, and V_e is the molar volume of the dry electrolyte. These molar volumes are given by [60]

$$V_\mathrm{w} = \frac{M_{\mathrm{H_2O}}}{\rho_\mathrm{l}},$$

where ρ_l is the density of liquid water and

$$V_\mathrm{e} = \frac{\mathrm{EW}}{\rho_{\mathrm{m,\,dry}}}.$$

Ge et al. [59] measured the water flux across the catalyst-coated membrane in an in-operando cell and estimated the absorbed-water diffusivity prefactor α_λ to be $2.72 \cdot 10^{-5}$ cm^2/s. However, they assumed infinitely thin catalyst layers, and thus the given value may not be representative of the back-diffusion of water in either membranes or catalyst layers. Moreover, electro- and thermo-osmosis were neglected, which might have affected the estimated water diffusivity.

In this work, an α_λ value of $5.44 \cdot 10^{-5}$ cm^2/s was found to provide a sufficient agreement with the experimental resistance dynamics. The effect of the absorbed-water back-diffusion coefficient on the dynamic behavior of fuel cells is analyzed later in this work.

Membrane. Motupally et al. [65] provided a relation for the diffusion coefficient of water absorbed into the membrane that was commonly used in later modeling publications [42,49,79,81]. Ge et al. [59] estimated a higher diffusivity when the finite-rate exchange between the water in the ionomer and in the pores was accounted for (it was neglected by Motupally et al.). However, as discussed earlier, the simplifying assumptions made by Ge et al. might have affected their estimated hydration parameters. In this work, a scaled version of the electrolyte-water diffusion coefficient proposed by Motupally et al. [65] was used (shown in Table 6). A constant factor of 3.2 was introduced to scale the back-diffusion of water in the membrane in order to match the experimental resistance dynamics. Analysis

of the effect of the absorbed-water diffusivity in PEM on the fuel-cell dynamics is shown later in this work. The detailed analysis of the water uptake by Nafion® membranes and the related water diffusivity can be found in the Supplementary Information

2.5.3. Kinetics of water absorption and desorption by the electrolyte

The absorption/desorption rates for the electrolyte water were calculated using [13,59]

$$k_\lambda = \frac{\alpha_{\text{abs/des}}}{L_{\text{CL}}} f_{\text{V}} \exp\left[\frac{20000}{R}\left(\frac{1}{303} - \frac{1}{T}\right)\right], \tag{10}$$

where $\alpha_{\text{abs/des}}$ (cm/s) is the rate constant for absorption ($\lambda < \lambda_{\text{eq}}$) or desorption ($\lambda > \lambda_{\text{eq}}$).

The interfacial electrolyte-water transport rate $\alpha_{\text{abs/des}}$ was reported to vary between 10^{-5} and 10^{-1} cm/s depending on relative humidity, temperature, and thickness of the ionomer [93,95]. These values may not all be valid for the water absorption/desorption kinetics in the catalyst layers since they were obtained for relatively thick, unconstrained electrolyte membranes [93,95] or for thin films deposited on metals and quartz crystals [92,93] instead of carbon. The absorption/desorption rates of water by the electrolyte in a fuel-cell MEA were experimentally estimated by Ge et al. [59] to be $1.14 \cdot 10^{-5}$ cm/s and $4.59 \cdot 10^{-5}$ cm/s, respectively, with an Arrhenius-type temperature correction. However, a recent transient-modeling publication by Goshtasbi et al. [13], who used the absorption/desorption coefficients from Ge et al., showed a 100% deviation from the experimentally measured 10-kHz impedance of the cell. Therefore, these coefficients were treated as fitting parameters in this work, using the values reported by Ge et al. [59] as the baseline. The values of the absorption and desorption rates estimated from the experimental resistance dynamics were $4.59 \cdot 10^{-5}$ cm/s (about 4 times higher than in reference [59]) and $41.31 \cdot 10^{-5}$ cm/s (9 times higher), respectively. A parametric study on the electrolyte-water-exchange rates is shown later in this work.

2.5.4. Amount of water produced electrochemically directly in the electrolyte phase

Since the catalyst surface is at least partially covered by the electrolyte in the catalyst layers, it is reasonable to assume that some water may be produced at the catalyst surface under the ionomer film, into which it is then directly absorbed. The amount of water that may directly enter the ionomer has not been measured experimentally. The simulations exhibited high sensitivity, especially in the predicted ohmic resistance, to the amount of water set to be produced in the electrolyte phase. In this work, a good agreement with the experimental resistance data was achieved when 3% of water was assumed to be produced in the electrolyte phase.

An order-of-magnitude analysis of the ORR-water-production and the water-absorption source terms[a] shows that the rate of water absorption from the gas phase is up to 4 orders of magnitude lower than the rate of the electrochemical production of water depending on the current density. It is reasonable to expect that there exists some resistance to the uptake of the water that was produced electrochemically at the catalyst-ionomer interface. Such resistance may be approximated by introducing a rate constant to the water-production source term in the electrolyte. That rate constant is not known experimentally, and it was assumed in this work to have the value of unity. The small amount of water set to be produced inside of the electrolyte to match the experimental resistance curves can be explained by the shown difference in the order-of-magnitude of the ORR-water production and absorption

from vapor, as well as the absence of a limiting rate constant.

2.5.5. Local oxygen-transport resistance in the catalyst layers

The experimental value for the oxygen-dissolution rate constant k_{O_2} used in the ICCP model can be estimated by fitting the oxygen-transport resistance and limiting current density [43,96]. Previously, Secanell et al. [43] found k_{O_2} to be 10^{-3} m/s using a steady-state PEMFC model similar to what is described in this publication. In this work, the value of this rate coefficient was estimated by comparing the experimental and numerical limiting current density with 1% oxygen supply. The resulting value of k_{O_2} was $4.7 \cdot 10^{-4}$ m/s.

2.6. Solution approach

The model presented in this work was implemented in the in-house, open-source software for fuel cell modeling, OpenFCST [97,98]. For the temporal discretization, implicit Euler method was used with a constant time step of 0.25 or 1 s in the polarization-curve simulations and with an automatic time-stepping based on Richardson extrapolation [99,100] with a relative solution-error tolerance of 10^{-3} in the EIS simulations. Spatial discretization was performed using the finite-element method with second-order Lagrange shape functions and 16,350 degrees of freedom (2,725 mesh nodes). The nonlinear problem was linearized with Newton's method and a relative solution-error tolerance of 10^{-4} was used. Time-step-size and mesh-independence studies were performed to ensure the numerical accuracy of the solution.

Polarization-curve simulations were performed by applying 2 to 3 voltage sweeps at 0.44 mV/s (equivalent to the experimental voltage steps of 20 mV each 45 s). A computationally efficient EIS approach proposed by Bessler [101] was used to simulate impedance spectroscopy. The DC solution was obtained by performing a steady-state simulation. Then, a rapid linear ramp of 1 mV over 10^{-9} s was applied in voltage at $t = 0$, after which the voltage was held constant. Voltage and current density were recorded with the time-step size gradually increasing by 0.1% between the time layers from 10^{-10} to 10^{9} s until the time $t = 10^{10}$ s was reached. A non-equispaced Fourier transform suggested by Wiese and Weil [102] was performed on both voltage and current-density data, and the ratio of their Fourier transforms was computed to give impedance. This approach allows the extraction of a whole impedance spectrum (in this work - at 10^{-6}–10^{6} Hz) from a single simulation, which reduces the computational time compared to the conventional sine-wave-based EIS approach, where the spectra are obtained frequency-by-frequency. The rapid-EIS approach was validated by Bessler [101] and shown to produce the same spectra as the sine-wave approach. A similar study was performed in this work to validate the implementation of the rapid-EIS approach and the Fourier transform and is shown in the Supplementary Information

[a]Production of water in ORR:

$$\frac{j}{2F} = \frac{i}{2L_{\mathrm{CL}}F} = \mathcal{O}\left(\frac{1\ \mathrm{A/cm^2}}{1\ \mathrm{mol_{e^-}/mol_{H_2O}}\ 10^{-4}\ \mathrm{cm}\ 10^{5}\ \mathrm{C/mol_{e^-}}}\right) = \mathcal{O}\left(0.1\right)\ \mathrm{mol_{H_2O}/(cm^3\,s)};$$

Absorption of water by the electrolyte:

$$\varepsilon_{\mathrm{m}}\frac{k_{\mathrm{abs}}}{L_{\mathrm{CL}}}\frac{\rho_{\mathrm{m,\,dry}}}{\mathrm{EW}}(\lambda_{\mathrm{eq}}-\lambda) = \mathcal{O}\left(0.1\frac{10^{-5}\ \mathrm{cm^2/s}}{10^{-4}\ \mathrm{cm}}\frac{1\ \mathrm{g/cm^3}}{10^{3}\ \mathrm{g/mol_{SO_3^-}}}1\ \mathrm{mol_{H_2O}/mol_{SO_3^-}}\right) = \mathcal{O}\left(10^{-5}\right)\ \mathrm{mol_{H_2O}/(cm^3\,s)}.$$

The simulation time varied between 8 and 27 hours for the polarization-curve simulations depending on the voltage range, time-step size, and the number of the performed sweeps. Each EIS simulation took 2 to 4 days. All simulations were performed in parallel using 4 threads of Intel® Xeon® E5-2690 v2 CPU at 3.00 GHz.

3. Experiment

3.1. Fuel cell fabrication

The membrane-electrode assemblies were manufactured by inkjet-printing following the protocol described in references[96,103,104]. A mixture of 37.5 mg of 40 wt% Pt/C catalyst (HySa-K40 on Ketjenblack® EC300J, HyPlat), 37.3 ml of Nafion® ionomer solution (Liquion 5 wt% LQ-1105, Ion Power), 1.9 ml of 2-propanol (99.5%, Fisher Scientific), and 1.6 ml of propylene glycol (99.5%, Sigma-Aldrich) was prepared to obtain a catalyst ink with a 30 wt% Nafion® loading. The 5-cm^2 catalyst layers were directly deposited on a 25.4-μm thick Nafion® membrane (NR-211, IonPower) with a commercial piezoelectric inkjet printer (Fujifilm Dimatix DPM-2800). Catalyst loading was controlled by means of the number of the printed layers on the membrane. For the cathode side, a loading of 0.15 $\mathrm{mg_{Pt}/cm^2}$ was used. Once the CCL was printed, it was left to dry overnight before printing the ACL. The anode side had a catalyst loading of 0.10 $\mathrm{mg_{Pt}/cm^2}$. Each printed layer was inspected in an optical microscope to ensure there were no major cracks. Scanning-electron microscopy (SEM) was also used to verify the uniformity of the catalyst-layer structure.

Catalyst-layer thickness was measured from the cross-sectional SEM images. The average thickness was 4.50 ± 0.19 µm for the cathode side and 2.81 ± 0.11 µm for the anode side. The catalyst-coated membrane (CCM) was sandwiched between two 5-cm^2 SGL 29BC carbon-paper layers (GDL and MPL, Sigracet) and two graphite bipolar plates with a parallel-channel configuration. Rigid, 150 µm-thick PTFE gaskets were used to control the diffusion-media thickness and to seal the cell to avoid gas leakage.

3.2. Electrochemical characterization

A Scribner 850e test station and a Bio-Logic SP-300 potentiostat were used to carry out the electrochemical characterization of the cell. First, the cells were conditioned at 80 °C with hydrogen and air at 80% RH for 16 one-hour-long steps from 0.1 to 5 A with 30-second OCV intervals between each step. Before each test, a preconditioning was performed at the given operating conditions by holding the cell voltage at 0.6 V for 30 min.

Electrochemical surface area (ECSA) was calculated by the means of cyclic voltammetry (CV) at 30 and 80 °C using fully humidified hydrogen and nitrogen as the anode and cathode gas supply, respectively. The hydrogen-adsorption and desorption peaks (between 0.05 and 0.4 V) resulted in an ECSA of 58.1 ± 9.5 $\mathrm{m^2_{Pt}/g_{Pt}}$ based on the measurements of three cells. The double-layer capacitance baselines were computed from the non-faradaic process region of the CV (between 0.3 and 0.6 V) following the methodology in reference[105]. The measured double-layer capacitance value was 24.1 ± 1.2 $\mathrm{mF/cm^2}$.

Polarization curves were obtained at 80 °C using hydrogen in the anode and 1, 10, 21, and 100% oxygen-in-nitrogen mixture in the cathode, with both streams humidified to 50 and 70% RH. The gas-flow rates were fixed at 0.2 and 1.0 slpm for hydrogen and oxygen, respectively, resulting in stoichiometry of 4.5–4.8 (H_2) and 0.4–48 (O_2) at 1 $\mathrm{A/cm^2}$. In all tests, a backpressure of 50 kPa was applied and controlled by an automatic backpressure

regulator (Scribner 850BP). The scans were performed with the Scribner test station in the potentiodynamic mode from OCV to 0.05–0.2 V in 20-mV steps every 45 s and verified with 0.44 mV/s scans with the Bio-Logic potentiostat. Current-interrupt-based resistance was measured during the experiments performed with the Scribner station.

The EIS tests were performed in the galvanodynamic mode by applying a sinusoidal perturbation with an amplitude of 3–4% of the current for a frequency range of 100 kHz–0.1 Hz. The spectra were measured at 0.1, 0.4, 0.7, 1.0, and 1.4 A/cm^2 holding the desired current for 3–5 min before each test to let the cell stabilize and to minimize voltage drift. After the data were gathered with increasing current between the tests, the experiments were repeated in the reversed order to ensure no significant polarization-hysteresis effect on the impedance spectra. The impedance-spectrum and polarization-curve data were verified for consistency by comparing the measured voltage-current relationships.

Linearity of the measured spectra was checked with the Kramers-Kronig test, which is also used as a test for stability and causality of the analyzed system[106,107]. The Kramers-Kronig relations allow to reconstruct the real part of impedance from its imaginary part and vice versa[106,107]:

$$\mathrm{Re}(\hat{Z}(\omega)) = \lim_{\hat{\omega}\to\infty} \mathrm{Re}(Z(\hat{\omega})) + \frac{2}{\pi}\int_0^\infty \frac{\hat{\omega}\,\mathrm{Im}(Z(\hat{\omega}))}{\omega^2-\hat{\omega}^2}d\hat{\omega}, \tag{11}$$

$$\mathrm{Im}(\hat{Z}(\omega)) = -\frac{2}{\pi}\int_0^\infty \frac{\omega\,\mathrm{Re}(Z(\hat{\omega}))}{\omega^2-\hat{\omega}^2}d\hat{\omega}. \tag{12}$$

Residuals between the original and the reconstructed impedance were defined as[107]

$$\delta_{\mathrm{Re}}(\omega) = \frac{|\mathrm{Re}(\hat{Z}(\omega)) - \mathrm{Re}(Z(\omega))|}{|\hat{Z}(\omega)|}, \tag{13}$$

$$\delta_{\mathrm{Im}}(\omega) = \frac{|\mathrm{Im}(\hat{Z}(\omega)) - \mathrm{Im}(Z(\omega))|}{|\hat{Z}(\omega)|}. \tag{14}$$

Note that the Kramers-Kronig relations (11) and (12) require integration over frequencies ranging from 0 to ∞. The maximum relative difference between the original and the reconstructed spectra was under 9%, which was considered sufficient given the constrained frequency range used in the experiments.

All measured spectra exhibited a high-frequency inductive behavior due to cables and were inductance-corrected. The high-frequency portion of each spectrum with positive imaginary impedance values was first fitted with an impedance of an inductor-resistor circuit using the Bio-Logic EC-Lab® software. Then, impedance of an inductor with the fitted inductance of 11.6 ± 0.3 nH was computed for the whole frequency range and subtracted from the original data.

3.3. Effect of oxygen concentration and stoichiometry on fuel-cell impedance spectra

Bipolar plates with a parallel-channel configuration were chosen as they allow to limit the number of the modeled dimensions to two by considering a cross-section of the cell instead of its full three-dimensional geometry[55]. Depending on the goals of the study, either along-the-channel or through-the-channel models can be used[55]. Along-the-channel models[31,38–40,81,108,109] account for the reactant depletion and water accumulation along the parallel channels of the flow field, but are unable to predict the channel-land interaction, which may be significant in fuel

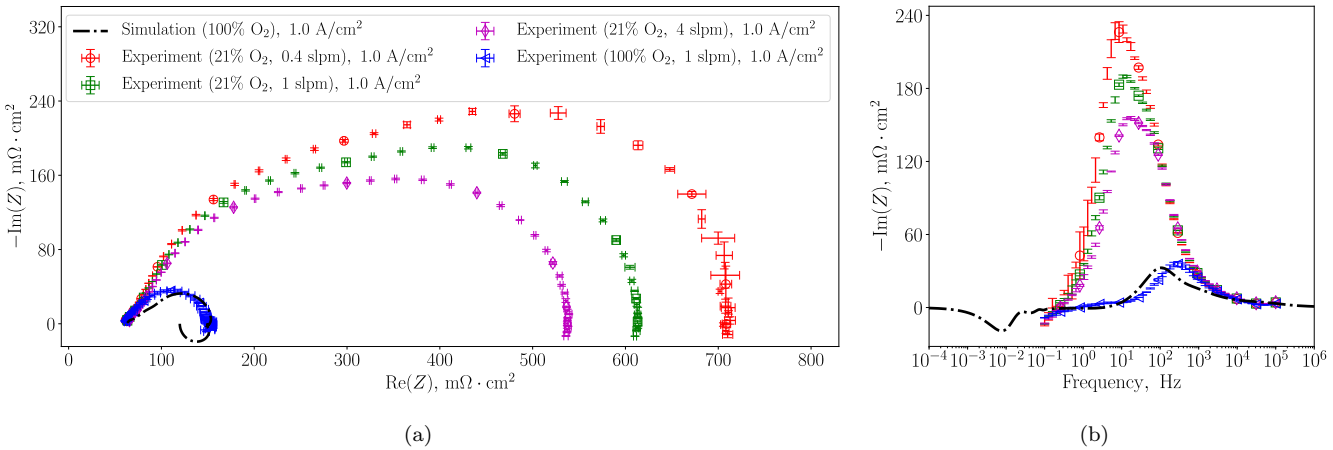

Figure 2: Effect of the cathodic flow composition and rate on the impedance spectrum at 1 A/cm^2: (a) Nyquist plots and (b) Bode plots of the imaginary part. Oxygen stoichiometry was about 4.1, 10, and 41 in air and 48 in the pure-oxygen case. The cell was operated at 80 °C, 50% RH, and 1.5 atm.

cells[110]. A number of through-the-channel models[42,45,49,83,111,112], including the model in this work, have been developed in the past relying on the concept of a "differential cell"[3]. It is believed that under the "differential" conditions, i.e., high flow rates with stoichiometry above 10, the variation in the reactant concentration and water accumulation along the parallel channels of the cell are eliminated[3]. These conditions allow to analyze the performance of the MEA independently of the flow field and thus are ideal for through-the-channel models as those do not take the along-the-channel dimension of the cell into account.

In this work, the experimental cell was initially operated with a humidified hydrogen flow in the anode channel at 0.2 slpm (stoichiometry of 4.8 at 1 A/cm^2) and a humidified air flow in the cathode channel at 0.4 slpm (oxygen stoichiometry of 4.1 at 1 A/cm^2). Under such conditions, a second capacitive arc was observed in the impedance measurements, which the model failed to predict with any given set of input parameters: no variation in the mass, heat, or charge-transfer parameters induced that additional impedance arc. The appearance of an additional capacitive arc in the fuel-cell impedance spectra has been attributed to along-the-channel mass transport in the modeling literature[31,38,39], and so the experiments were repeated with higher cathodic flow rates. The second arc of the measured spectra shown in Figure 2 decreased with an increase in the cathode flow rate, confirming the relation of the arc to the along-the-channel transport. The arc, however, did not disappear even when oxygen-in-air stoichiometry was increased to 41 at 1 A/cm^2. The inability to eliminate the channel effects is in agreement with the results of a numerical study by Balen[113] that showed oxygen depletion and water vapor accumulation along the fuel-cell channel in a parallel-channel configuration even at stoichiometry as high as 10.

An appropriate choice of the operating conditions had to be made in order to obtain experimental data with which the model could be validated, and thus all impedance spectra in the validation section of this work have been measured with a pure oxygen supply in the cathode. Passing pure oxygen through the cathode channel at 1 slpm resulted in a stoichiometry of about 48 at 1 A/cm^2. The along-the-channel arc was minimized in the obtained spectra, as illustrated in Figure 2 at 1 A/cm^2, where the simulated spectrum is also shown for comparison.

The observations made above indicate that achieving operation close to the "differential" mode might require a stoichiometry significantly exceeding the recommended minimum value of 10 (see reference[3]). Since the "differential"

mode was not possible to achieve in our laboratory with the air flow, pure oxygen was used to ensure the experimental EIS data were gathered under the conditions suitable for validating the model in use.

4. Results and discussion

4.1. Model validation

Experimental and simulated polarization and ohmic-resistance curves at varying oxygen concentration are shown in Figure 3. The ohmic resistance was measured using the current-interrupt and EIS techniques, and thus only contained the high-frequency portion of the resistance. Ohmic resistance was computed in the model through ohmic heating as[43,114]

$$R = \frac{1}{i^2 A^2} \int \left(\sigma_{\mathrm{s}} \nabla \phi_{\mathrm{s}} \cdot \phi_{\mathrm{s}} + \sigma_{\mathrm{m}} \nabla \phi_{\mathrm{m}} \cdot \phi_{\mathrm{m}} \right) \, dV, \tag{15}$$

where i is the current density in A/cm^2, A is the in-plane area of the cell, and V is the volume of the integration domain. For that, only the membrane, gas-diffusion layers, and micro-porous layers were included in the resistance calculation carried out with equation (15) as the resistance of only those layers is believed to comprise the HFR[16,17,32,44]. The electronic resistance of the catalyst layers was also included in the resistance calculation, but was negligible compared to the ohmic resistance of other components. Contact resistances were not directly considered in the model as the overall agreement with the experimental resistance (shown later) negated the necessity of modifying the conductivity values of the cell components. The experimentally measured contact resistance between the MEA components was about 1.3 $\mathrm{m\Omega \cdot cm^2}$ with the additional resistance of the bipolar plates and the current collectors of approximately 8.7 $\mathrm{m\Omega \cdot cm^2}$.

The experimental current-interrupt-based resistance is known to overestimate the EIS-based HFR[44]. Therefore, the model's ability to predict the ohmic resistance of the cell was validated with the experimental HFR values. Agreement within about 3% was achieved between the experimental EIS-based HFR and the simulated ohmic-heating-based equivalent. The latter will also be referred to as HFR in this work.

Oxygen content in the cathode channel prior to humidification was varied between 1% and 100%. As mentioned earlier, the 1% oxygen case was used to estimate the local oxygen transport resistance in the catalyst layers (i.e., the $k_{\mathrm{O_2}}$ rate constant), and the 100% oxygen case was used to estimate the hydration-related parameters (absorption/desorption rates, absorbed-water-diffusivity prefactor, and the amount of water produced in the ionomer phase). The current density was limited to about 1.8 A/cm^2 in the latter case to avoid flooding of the cell with product water.

Good agreement was achieved in both limiting current density at 1% oxygen and the HFR at 100% oxygen. The drop in the resistance due to electrolyte hydration was similar between the model and the experiments. It can be seen as well in Figure 3(b) that the predicted HFR remained the same at the same current density when the oxygen content in the cathode channel was varied unless mass-transport limitations were observed. This is as expected since the rate of water production, and thus the rate of the electrolyte hydration, should be approximately the same at the same current density. The observed agreement with the experimental data validates the model's capability to predict single-phase mass transport losses and hydration of the electrolyte.

Even though only the first full sweep is shown in both the simulated and the experimental data, two to three subsequent sweeps have been performed in all cases, both simulated and measured, to ensure no drift in the performance

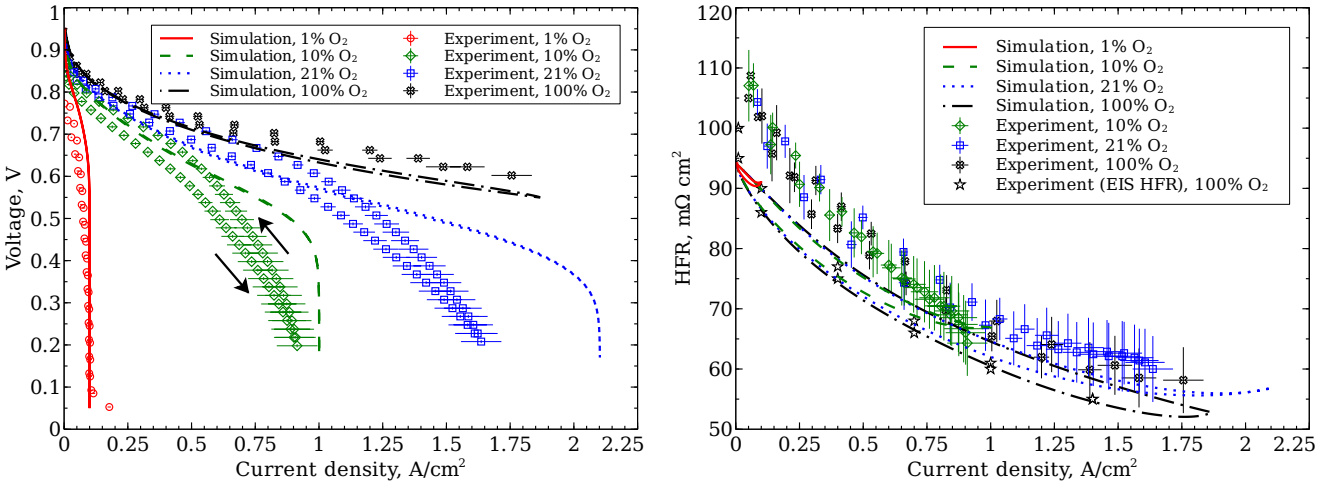

Figure 3: Comparison of the simulated and experimental polarization (a) and HFR (b) curves with varied oxygen content in the cathode channel (prior to humidification). Only the first sweep is shown. Error bars in the experimental data represent standard deviation estimated from three tested cells. The cell was operated at 80 °C, 50% RH, and 1.5 atm.

or the resistance between the sweeps. This was important in the experiments to make sure the cell was correctly conditioned prior to the experiment and no transient history, such as hydration, affected the measurements. In the simulations, no drift between the sweeps meant that the time scales of the major cell responses were correct and the stable performance was achieved within one sweep, as seen in the experiments.

The predicted polarization-curve hysteresis was significantly lower than that observed in the experimental data; its largest magnitude varied between 10 and 40 mA/cm^2 at 0.7 V in the simulations, but was 130–200 mA/cm^2 in the experimental data. The simulated resistance hysteresis, however, was similar to the experiments, e.g., depending on the oxygen concentration, hysteresis magnitude was 1–4 m$\Omega\cdot$cm^2 at 0.75 A/cm^2 in the model and 1–3 m$\Omega\cdot$cm^2 in the experimental data. Therefore, the larger polarization hysteresis in the experimental data in Figure 3(a) was not associated with the HFR hysteresis. The model also overpredicted the cell performance at the intermediate oxygen contents (10% and 21%). The discrepancies in the predicted performance and polarization hysteresis at these oxygen contents may be because it was not possible to achieve a high enough flow rate in the experiments to avoid the additional mass transport losses due to the oxygen depletion and liquid water accumulation along the parallel channels. In addition to the along-the-channel effects, this may have been a result of neglecting, for instance, the transient terms in the reaction kinetics sub-model, e.g., in the formation of the platinum oxides that may also lead to hysteresis. Furthermore, the double-trap ORR model[51] used in this work predicts the reaction order (with respect to oxygen) of about 0.3–0.5, which is significantly lower than the experimentally measured order of about 0.8–1[96,115,116] and affects the dependency of the simulated current on oxygen concentration[51b]. Liquid-water formation in the MEA may have also been the reason for the observed performance discrepancy[114].

Next, the model's ability to predict the changes in the ohmic resistance with RH was verified by comparing the simulated polarization and HFR curves to the experimental data obtained at 50% and 70% RH with 21% oxygen. The

[b] A more advanced multi-step ORR model presented recently by Jayasankar and Karan[116] is able to predict the correct reaction order.

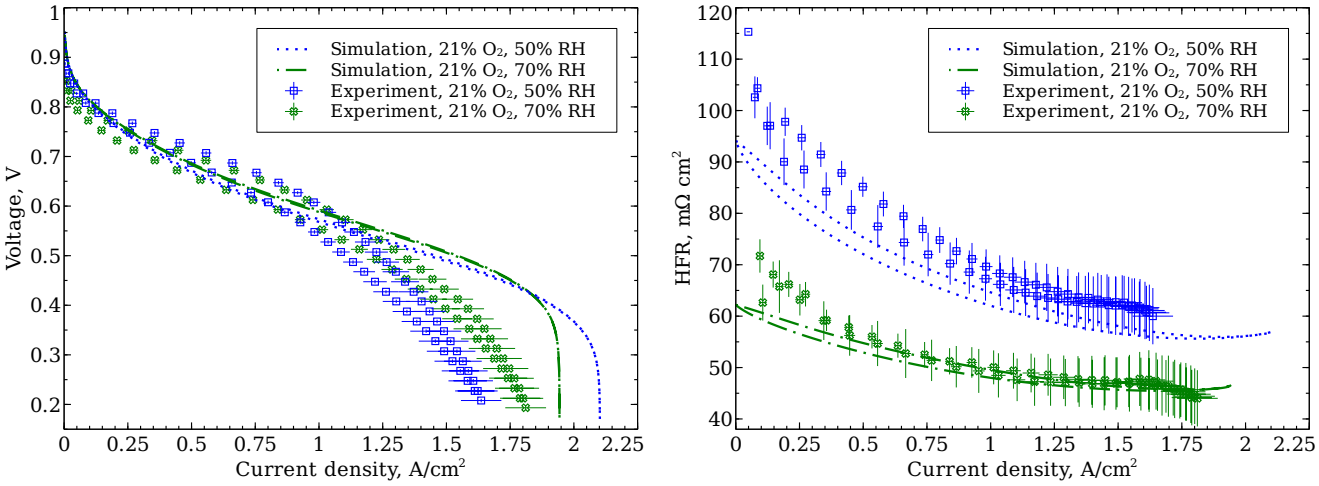

(a) (b)

Figure 4: Comparison of the simulated and experimental polarization (a) and HFR (b) curves with varied RH. Only the first sweep is shown. Error bars in the experimental data represent standard deviation estimated from three tested cells. The cell was operated at 80 °C, 50% RH, 1.5 atm, and 21% oxygen in the cathode flow (prior to humidification).

comparison with the experimental data is shown in Figure 4. The resistance drop with increased RH in Figure 4(b) was similar to that in the experiments. The predicted resistance hysteresis also remained similar to that in the experimental data. Apart from the along-the-channel and liquid-water effects that the model could not capture at the current density approximately above 0.75 A/cm^2, it can be seen from Figure 4(a) that the performance predictions are in reasonable agreement with the experimental data. Interestingly, simulations showed that the 70% RH case had more mass transport losses compared to the 50% RH case; this trend was opposite to that observed in the experiment, which strengthens the hypothesis that liquid water might have played a role at high current density. A lower limiting current density was achieved due to the lower oxygen content in the cathode after the humidification.

Finally, predicted and measured impedance spectra were compared in the pure-oxygen case at varying current density. This validation was conducted with the same, single parameter set that was used in the simulations shown in Figures 3 and 4, making it the second independent validation of the model with a different type of transient analysis.

The rapid EIS approach discussed earlier was used to compute the impedance spectra. Since the model was operated in the potentiodynamic mode, the cell voltages producing the current densities from the EIS experiments were found in the model, and the spectroscopy was simulated at those potentials. The magnitude of the perturbation was chosen sufficiently small in both the experiments and the model so as not to deviate significantly from the operating point and to ensure the linearity of the dynamic response, and, at the same time, not too small to avoid large noise-to-signal ratio. Thus, the approaches taken in the measurements and the simulations were assumed equivalent, even though obtained through different modes (galvano- and potentiodynamic). Linearity of the simulated spectra was verified with the Kramers-Kronig relations (11) and (12). Relative residuals defined in equations (13) and (14) were below 1% for the simulated and the reconstructed spectra.

The simulated and the experimental spectra are shown in Figure 5 along with the respective polarization and HFR curves. A good overall agreement was achieved in the impedance spectra in the current-density range between 0.1 and 1.4 A/cm^2. A significant deviation was, however, observed between the simulated and the measured spectra

in the high-frequency portion, where the spectrum is known to be associated with the double-layer and electrolyte-conductivity dynamics[17,19,26,30,34,38]. Parametric studies on the hydration-related parameters discussed later in this work show that water management has a significant effect on the impedance spectrum at high frequencies. At the same time, varying the double-layer capacitance in the model resulted in no change in the Nyquist plot (Figures 5(a) and 5(c)), but the halved capacitance shifted the capacitive peak in the Bode plot (Figure 5(b) and 5(d)) closer to the experimental frequencies. This may indicate that the double-layer capacitance measured in a cyclic-voltammetry experiment at 100% RH may be an overestimation due to the RH-dependent catalyst-ionomer interfacial area[117,118].

The simulated spectra shown in Figure 5 deviated from the experimental data at high frequencies (of order 100 Hz and higher), and the magnitude of the deviation increased with current density. As it will be shown later in this work, the high-frequency portion of the fuel-cell impedance spectrum is highly dependent on the catalyst-layer electrolyte hydration and conductivity.

The capacitive behavior of the cell was accompanied by an inductive loop at about 0.1 mHz–6 Hz at moderate to high current densities. The nature of this low-frequency inductive behavior in the fuel-cell impedance spectra is discussed further in this work.

A distinctive feature of the spectra simulated at moderate to high current densities was the presence of impedance spirals between 0.02 and 1 Hz. These local impedance oscillations were equidistant in the Bode plot with about 50 mHz between the local extrema, indicating a resonance between the simulated hydration and conductivity dynamics of the membrane and the electrolyte phase of the catalyst layers (the effect of these phenomena on the impedance spectrum is discussed in this work). Even though the regions of the simulated spectra with local oscillations have all passed the Kramers-Kronig test and similar oscillations have been reported in both experimental[22] and modeling[37,119,120] studies (although at higher frequencies of 1-100 Hz[22,120] and attributed to the resonance between the oxygen transport along the channel and in the MEA[120]), a time-step-size analysis shown in the Supplementary Information revealed that the observed resonance was, at least in our case, a numerical artifact (the inductive behavior was, however, resolved with a sufficient degree of accuracy). This highlights the importance of verifying the unexpected impedance behavior by using a smaller time-step size in the simulations or a higher sampling frequency in the EIS experiments.

Another point of validation was the HFR extracted from the impedance spectra as

$$\mathrm{HFR} = \lim_{\omega \to \infty} \mathrm{Re}(Z(\omega)).$$

As seen in Figures 5(a) and 5(c), a good HFR agreement was achieved in all cases with both the EIS experiments (within about 3%) and the ohmic-heating-based values in Figure 3(b) (within about 1%). This validates the model's ability to predict the high-frequency resistance in the EIS and serves as another validation of the earlier computed ohmic resistance.

The DC resistance was found in the EIS simulations as

$$R_{\mathrm{DC}} = \lim_{\omega \to 0} \mathrm{Re}(Z(\omega)).$$

However, the lowest frequency used in the experiments (0.1 Hz) was not sufficient to observe the DC resistance. Instead, it was computed as the local negative slope of the polarization curve:

$$R_{\mathrm{DC}} = \frac{\partial \eta}{\partial i} = -\frac{\partial V}{\partial i}.$$

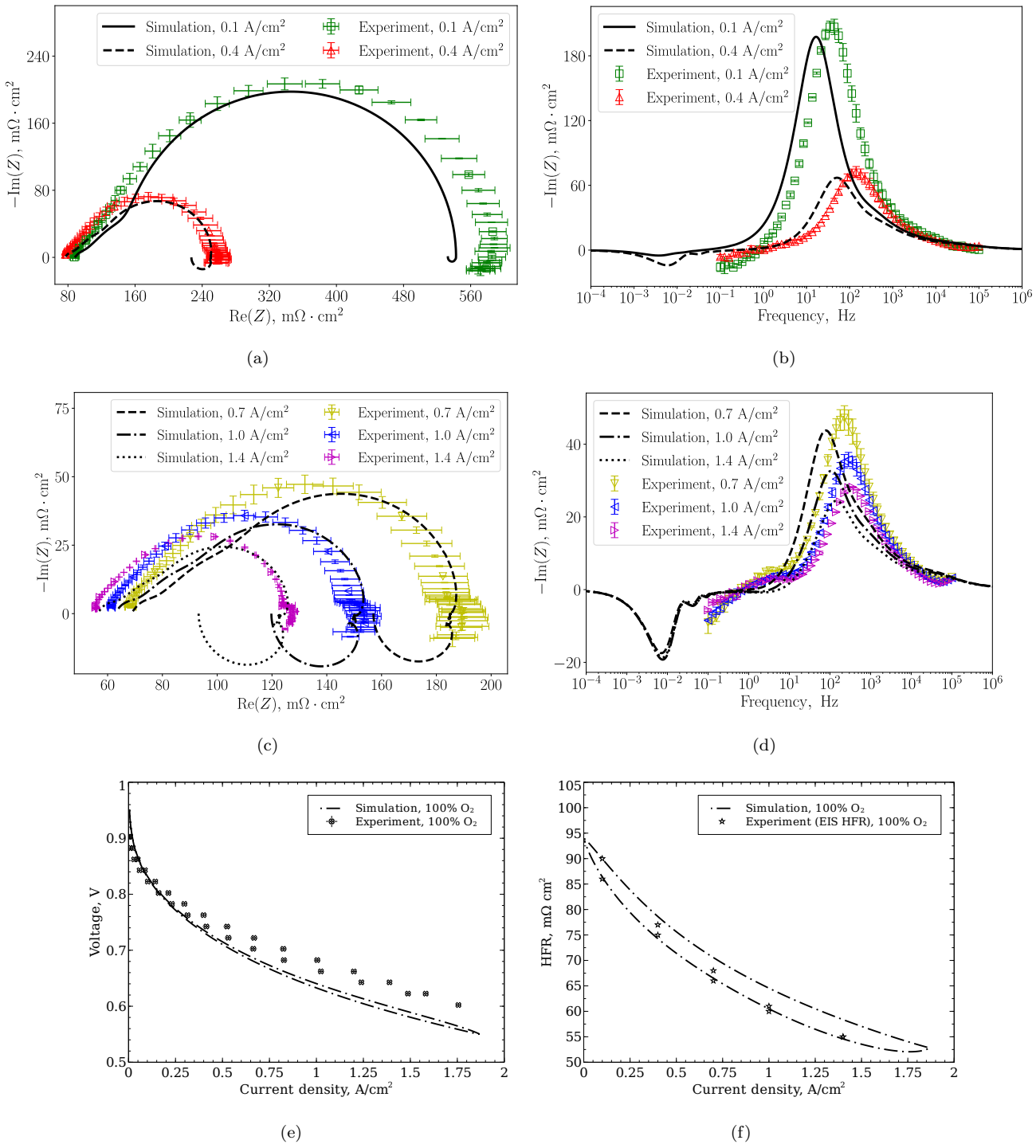

Figure 5: Comparison of the simulated and experimental impedance spectra: (a) and (b) Nyquist and Bode plots for the current density of 0.1 A/cm^2 and 0.4 A/cm^2; (c) and (d) Nyquist and Bode plots for the current density of 0.7 A/cm^2, 1.0 A/cm^2, and 1.4 A/cm^2. The corresponding polarization and HFR curves are shown in sub-figures (e) and (f), respectively. Only the first sweep is shown in sub-figures (e) and (f). Error bars in the measured spectra represent the standard deviation from two experiments. Error bars in the experimental polarization curve represent the standard deviation estimated from three tested cells. The cell was operated at 80 °C, 50% RH, 1.5 atm, and 100% oxygen in the cathode flow (prior to humidification).

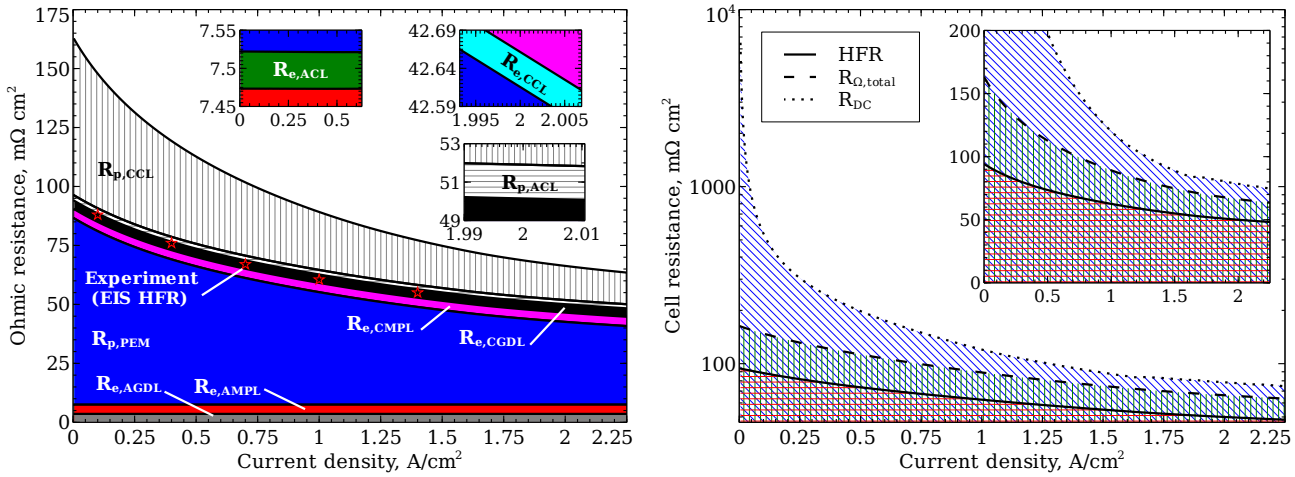

Figure 6: Breakdown of the simulated ohmic resistance (a) and cell resistance (b). Electronic and protonic resistances were marked R_{e} and R_{p}, respectively. The experimental EIS HFR data were taken from Figure 3(b) and averaged (the error bars represent the standard deviation). The cell was operated at 80 °C, 50% RH, 1.5 atm, and 100% oxygen in the cathode flow (prior to humidification).

A steady-state-polarization-curve simulation was considered as a true stationary reference for computing the DC resistance with the formula above. The deviation of the EIS-based DC resistance from that computed from the polarization curve was between 0.8% and 3% depending on the current density. Therefore, the EIS simulations were consistent with the polarization curves.

4.2. Ohmic-resistance breakdown

Before discussing the hydration-related parametric studies, an ohmic resistance breakdown is carried out for the pure-oxygen case from Figures 5(e) and 5(f) in order to verify that the HFR does not include the ionic resistance of the catalyst layers[16,17,32,44]. The ohmic-resistance breakdown is shown in Figure 6(a). It is clear that the HFR does not include the protonic resistance of the catalyst layers: the experimental HFR is in close agreement (within 3%) with the sum of the protonic resistance of the membrane and the electronic resistance of the other MEA components. The highly electronically conductive carbon-support phase of the catalyst layers forms a path of the least resistance for the current, and thus the significantly less conductive ionic phase does not appear in the HFR. The HFR composition is further confirmed by even closer, within 1%, agreement between the simulated HFR and the ohmic-heating-based resistance of the aforementioned layers. This study also validates the ohmic-heating approach for computing the individual ohmic resistances of the MEA components.

A comparison between the ohmic and DC resistance is illustrated in Figure 6(b). As current density increases, the DC resistance approaches the total ohmic resistance from Figure 6(a) in this case, where mass-transport losses are not dominant. The region of the graph with the blue stroke corresponds to the difference between the DC and the total ohmic resistance and corresponds to other losses, such as mass-transfer and charge-transfer resistance.

4.3. Water-management analysis

In the literature, the inductive behavior of fuel cells at low frequencies has been attributed to the electrolyte hydration[18,29,30], ORR intermediates[17,18,29], platinum oxide formation[29] or reduction[31], and carbon monoxide poi-

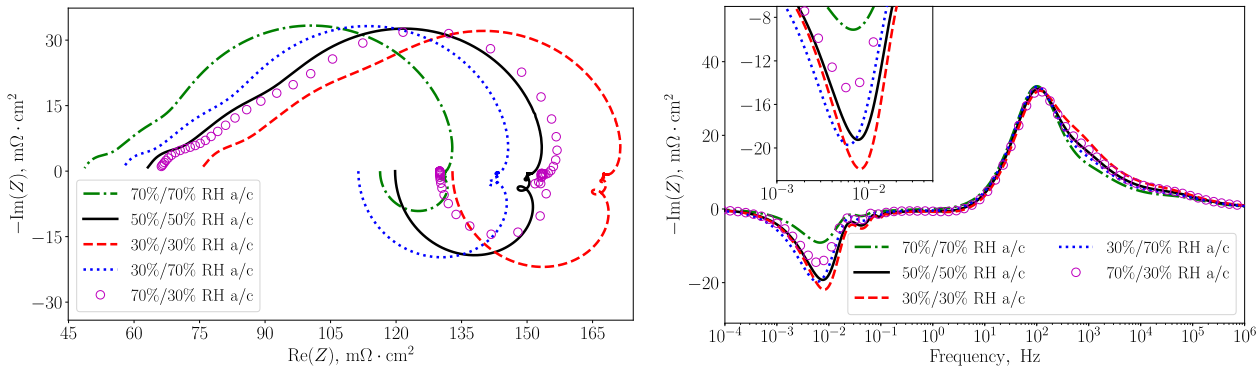

(a) (b)

Figure 7: Effect of relative humidity on the predicted impedance spectrum at 1 A/cm^2: (a) Nyquist plots, (b) Bode plots of the imaginary part. The cell was operated at 80 °C, 1.5 atm, and 100% oxygen in the cathode flow (prior to humidification).

soning[18]. In our model, however, the transient terms in the reaction-kinetics sub-models were neglected, and thus the dynamics of the ORR intermediates and platinum oxide could not be the cause of the inductive behavior in the simulated spectra. Carbon monoxide poisoning was also not modeled. The presence and the strength of the inductive behavior in the simulated spectra highly depended on the hydration-related parameters of the model. A number of parametric studies were performed in order to understand the effect of water management on the appearance of the low-frequency inductive loops in the impedance spectra. Current density of 1 A/cm^2 was chosen for these studies as the inductive behavior was sufficiently strong, as seen in Figure 5.

4.3.1. Effect of relative humidity

A study similar to the experimental RH imbalance analysis by Schiefer et al.[20] was carried out first to find if the model can correctly predict the trends in the inductive-loop-size dependency on RH. The spectra simulated at 1 A/cm^2 (as in reference[20]) with varied relative humidity in anode and cathode are shown in Figure 7(b), where the 50%/50% case is the reference taken from Figure 5. Similarly to reference[20], the lower RH of 30% in both compartments resulted in the largest inductive loop followed by the case with a higher cathode RH of 70% and the case with 50% RH in both sides (Figure 7(b)). The inductive loop was the smallest in the case of the highest RH of 70% in both anode and cathode. These observations validate the model predictions of the RH effect on the inductive loop and hint that the inductive behavior may be affected by the rate and direction of the water transport across the CCM. The additional case with 70% anode RH, 30% cathode RH, not considered in the reference study[20], resulted in the second-smallest inductive loop.

Figure 8 illustrates steady-state water-content distribution in the CCM at 1 A/cm^2. Interestingly, water content was higher in the 30%/70% anode/cathode RH case than in the 70%/30% RH case due to the insufficient back-diffusion of product water compared to electro-osmosis in the latter case. Water content in the CCM had a direct effect on the imaginary impedance at frequencies above 100 Hz, which increased by up to 54% between the symmetrical 70% RH and symmetrical 30% RH cases. At the same time, it had no direct correlation with the size of the inductive loop as evident from the imbalanced-RH cases. Thus, the low-frequency inductive behavior of fuel cells has a more complex nature rather than water distribution in the membrane and catalyst layers.

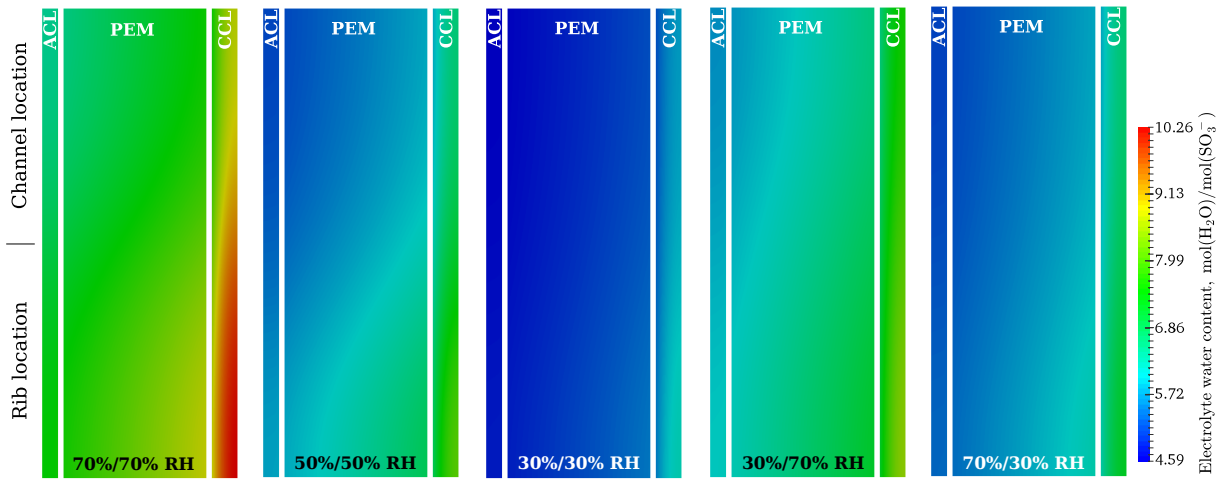

Figure 8: Comparison of the steady-state electrolyte-water-content distribution within the CCM at 1 A/cm^2 with varied RH in the anode and cathode compartments (the domains were scaled-up along the horizontal axis by a factor of 10 and gaps between the layers were added for clarity). The cell was operated at 80 °C, 1.5 atm, and 100% oxygen in the cathode flow (prior to humidification).

4.3.2. Effect of water absorption/desorption kinetics

A parametric study was performed on the rates of water absorption and desorption by the electrolyte in the catalyst layers to further investigate the nature of the low-frequency inductive loop of the fuel-cell-impedance spectra. The inductive loop was not present in the spectrum at 1 A/cm^2 with absorption/desorption rates reduced by a factor of 10^4 (compared to the reference case from Figure 5) as seen in Figure 9. The inductive loop became evident at about 0.1–20 mHz with the absorption/desorption kinetics from Ge et al.[59] (4 times slower absorption and 9 times slower desorption than in Figure 5) and reached its maximum in the reference case. As the water-exchange rates were further increased, the inductive loop gradually decreased in size and shifted to higher frequencies until reaching 10 mHz–6 Hz as seen in Figure 9 for the rates scaled up by 10^4 times. When vapor diffusivity in the porous layers was also increased by four orders of magnitude to quickly remove the product water, the inductive loop disappeared. This study indicates that the hydration-related inductive behavior of fuel cells depends on the dynamics of water absorption and desorption by the electrolyte.

Absorption/desorption kinetics of water also had a distinctive effect on the spectrum at frequencies between 100 Hz and 1 MHz. A direct relationship can be established between the strength of the capacitive behavior of fuel cells in that frequency range and the electrolyte-water exchange rates based on Figure 9(b). In alignment with the RH-imbalance study, a lower water content in the CCM observed with higher absorption/desorption rates (Figure 10) led to a stronger capacitive behavior of the cell as seen in Figure 9(b).

Figures 9(c) and 9(d) show that the water-exchange rates affected the polarization and HFR hystereses and magnitude. The larger the absorption/desorption rates and vapor diffusivity, the larger HFR and the lower performance were predicted as water produced directly in the electrolyte phase of the catalyst layers was allowed to desorb from the ionomer and leave the MEA faster. The largest hysteresis, up to about 40 m$\Omega \cdot$ cm^2, was observed with the rates from Ge et al.[59], in which case the quasi-stationary state was not achieved in one sweep, and, unlike the reference case and the experimental data in Figure 5, the cell exhibited an incomplete loop. A similar issue has been observed in the model by Goshtasbi et al.[13], who used the absorption/desorption rates of water from Ge et al.[59] and

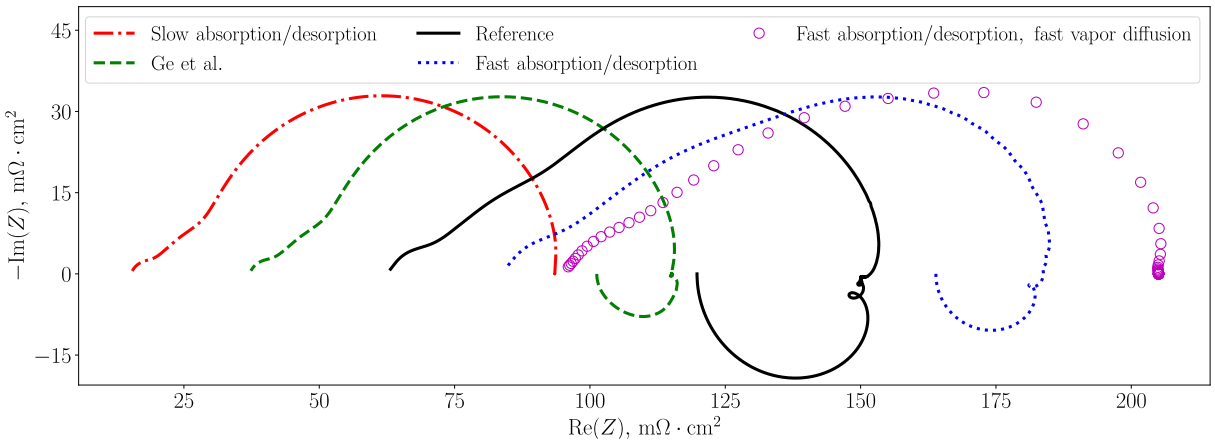

(a)

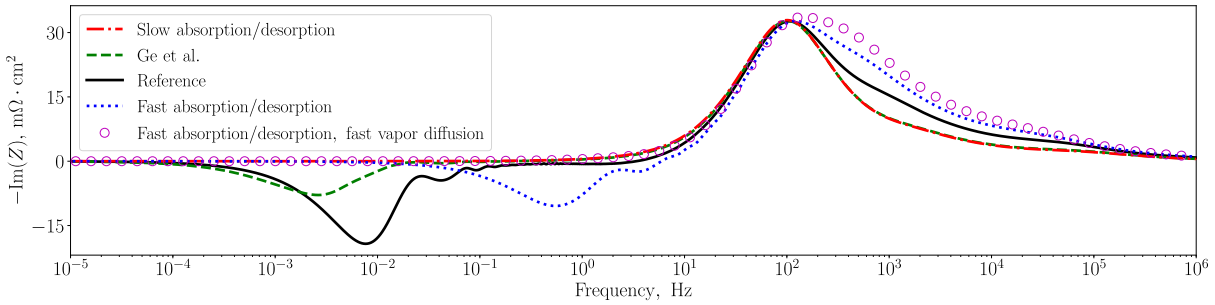

(b)

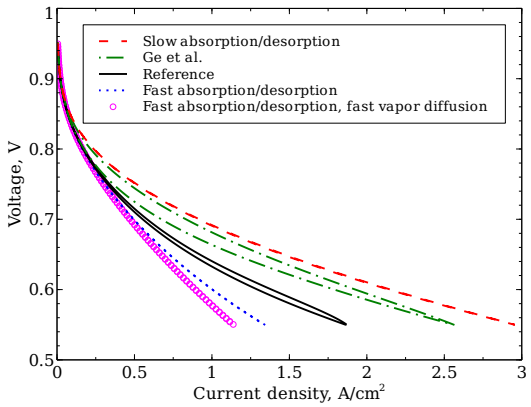

(c)

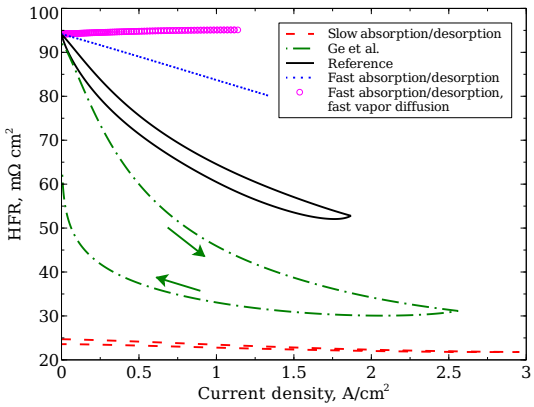

(d)

Figure 9: Effect of the rate of water absorption/desorption by the electrolyte on the predicted impedance spectra at 1 A/cm^2 (a,b), polarization curve (c), and HFR (d). The cell was operated at 80 °C, 1.5 atm, and 100% oxygen in the cathode flow (prior to humidification).

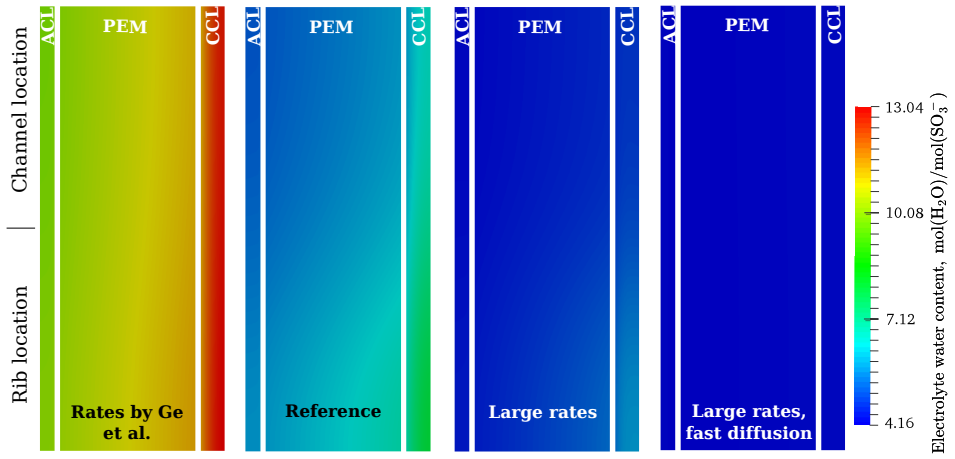

Figure 10: Comparison of the steady-state electrolyte-water-content distribution within the CCM at 1 A/cm^2 with varied water absorption/desorption rates (the domains were scaled-up along the horizontal axis by a factor of 10 and gaps between the layers were added for clarity). Left to right: rates by Ge et al.[59] ($\alpha_{\text{abs}} = 1.14 \cdot 10^{-5}$ cm/s, $\alpha_{\text{des}} = 4.59 \cdot 10^{-5}$ cm/s), reference case ($\alpha_{\text{abs}} = 4.59 \cdot 10^{-5}$ cm/s, $\alpha_{\text{des}} = 41.31 \cdot 10^{-5}$ cm/s), large rates ($\alpha_{\text{abs}} = 4.59 \cdot 10^{-1}$ cm/s, $\alpha_{\text{des}} = 41.31 \cdot 10^{-1}$ cm/s), and large rates with $D_{\text{w}}^{\text{eff}}$ scaled up by a factor of 10^4. The cell was operated at 80 °C, 1.5 atm, 50% RH, and 100% oxygen in the cathode flow (prior to humidification).

overpredicted the resistance by up to 2 times compared to the reported experimental data. This indicates that the water-exchange rates reported by Ge et al.[59] might be too low as the simulations do not agree with the experimental observations.

4.3.3. Effect of back-diffusion of water in the electrolyte

The nature of the two separate inductive loops in the fuel-cell impedance spectra was investigated further by modifying the water back-diffusion coefficient in the electrolyte. In this study, D_λ was scaled down by a factor of 3.2 first in the membrane, then in the catalyst layers, and finally in the whole CCM. Note that 3.2 was the scaling factor for the back-diffusion coefficient from Motupally et al.[65] as discussed in the modeling section.

The results of this parametric study at 1 A/cm^2 are shown in Figure 11. A lower back-diffusion coefficient led to a weaker inductive behavior at 0.1–200 mHz, especially in the catalyst layers. This aligns well with the earlier observation that this inductive loop is sensitive to anode and cathode RH (see Figure 7(b)). When the rate of back-diffusion was reduced in the whole CCM, the inductive process at 0.1–200 mHz was transformed into a capacitive process due to the increased role of electro-osmosis (a parametric study on the thermal osmosis of water in the PEM was also performed, but no significant change in the impedance spectrum was found at the considered operating conditions). In this case, the direction of the water-transport across the CCM was reversed to anode-to-cathode, and a significant anode dry-out took place (Figure 12), which resulted in the increase of the HFR at current densities approximately above 0.5–0.6 A/cm^2 with a reversed direction of the resistance hysteresis at higher current densities (Figure 11(d)) and a lowered performance (Figure 11(c)). These observations indicate that the inductive process at 0.1–200 mHz is affected by the individual mechanisms of water transport in the electrolyte. The reduced flux of the product water from cathode to anode leads to a decrease of the phase-lead of voltage, which weakens the inductive behavior. If the direction of water transport across the CCM is reversed, for example, due to stronger electro-osmosis, then the electrolyte cannot be sufficiently hydrated by the product water, as seen in Figure 12, to

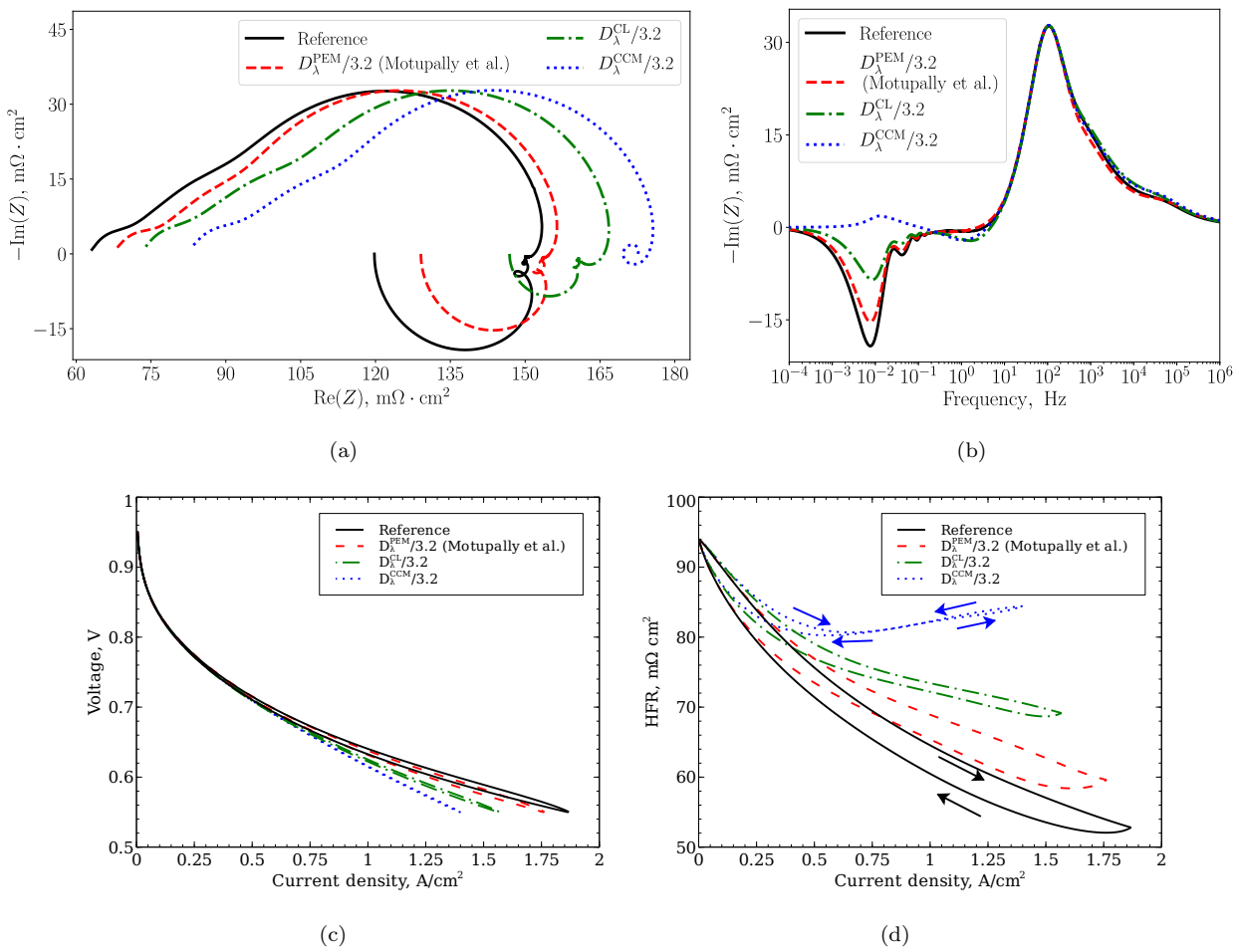

Figure 11: Effect of the coefficient of back-diffusion of water in the electrolyte on the predicted impedance spectra (a,b), polarization curve (c), and HFR (d). The cell was operated at 80 °C, 1.5 atm, and 100% oxygen in the cathode flow (prior to humidification).

support the voltage-phase-lead, and the dynamic behavior becomes capacitive.

In addition to the main inductive loop at 0.1–200 mHz, a second inductive loop at 0.2–5 Hz became apparent with the lower back-diffusion of water in CLs or the whole CCM as seen in Figures 11(a) and 11(b). Due to the lower rate of back-diffusion, more water was accumulated in the CCL while the ACL dried further (Figure 12), thus inducing more absorption and desorption of water. Note that this inductive process took place at frequencies similar to the "fast absorption/desorption" case in Figure 9(b). Therefore, this second process at 0.2–5 Hz is likely associated with the electrolyte-hydration dynamics in the catalyst layers rather than in the membrane, with a stronger effect of the better-hydrated CCL since the dominating behavior at the given frequencies is inductive.

5. Conclusion

An open-source, transient, single-phase 2D PEMFC model was presented in this work that is suitable for analyzing dynamic water management in fuel cells and its effect on their inductive behavior. A distinct feature of the model is its ability to reproduce the experimentally measured dynamic polarization, resistance, and impedance data with a single parameter set.

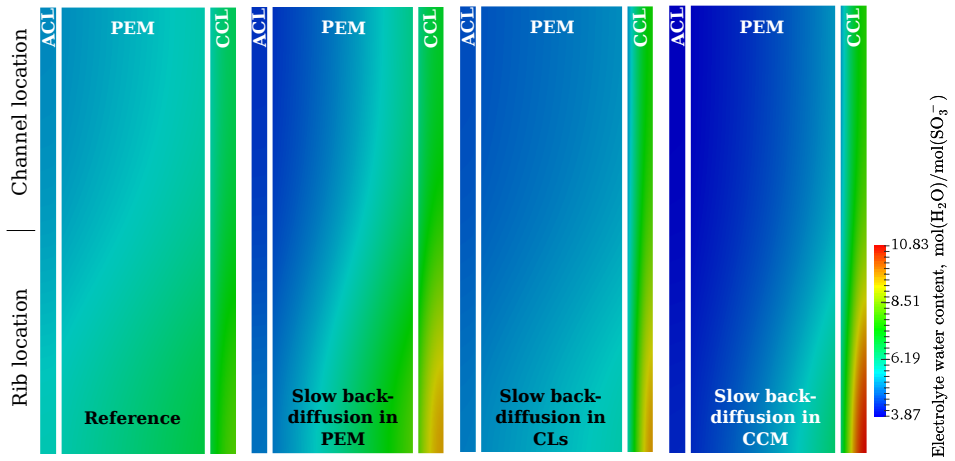

Figure 12: Comparison of the steady-state electrolyte-water-content distribution within the CCM at 1 A/cm^2 with varied back-diffusion coefficient of the absorbed water (the domains were scaled-up along the horizontal axis by a factor of 10 and gaps between the layers were added for clarity). Left to right: reference case, D_λ reduced by a factor of 3.2 in the membrane, D_λ reduced by a factor of 3.2 in the catalyst layers, and D_λ reduced by a factor of 3.2 in the whole CCM. The cell was operated at 80 °C, 1.5 atm, 50% RH, and 100% oxygen in the cathode flow (prior to humidification).

The developed model was used to perform a comprehensive analysis of the inductive phenomena observed in fuel cells, which has not been addressed in the literature with a detailed physical model. The study shows that there are two distinct inductive processes in the fuel-cell-impedance spectra that are related to the electrolyte hydration, one at 0.1–200 mHz and another at 0.2–5 Hz. Parametric studies performed in this work allow to deduce the nature of these inductive processes.

The first process occurring at 0.1–200 mHz strongly depends on the electrolyte-conductivity dynamics (mostly in the membrane) and is also affected by the water-transport mechanisms in the whole CCM. This inductive behavior only appears when non-zero rates of exchange of water between the electrolyte and the pores are used in the model. The size of the respective inductive loop directly depends on the magnitude of these rates and the ratio of the diffusive to osmotic fluxes of the absorbed water. If water back-diffusion is weak, this inductive process is transformed into a capacitive process. An inductive loop in this frequency range had been previously reported in experimental[20,29] and numerical[29,31] studies, and it can also be seen, in part, in the experimental data reported in this work.

The second process at 0.2–5 Hz induces a minor inductive loop of negligible size, which becomes larger when a stronger back-diffusion of water (weaker osmotic drag) is used in the model. The water-diffusion analysis shows that this loop is associated with the hydration and electrolyte-conductivity dynamics in the catalyst layers.

Water management was also shown to affect the high-frequency portion of the spectrum. Impedance at 100 Hz–1 MHz appeared to be highly sensitive to the interfacial water-exchange kinetics in the electrolyte of the catalyst layers, with a stronger capacitive behavior indicating faster interfacial transport of water and a lower water content in the electrolyte.

The ohmic-heating-based approach proposed by Secanell et al.[43] for calculating ohmic resistance of the individual fuel-cell components was validated in this work. The ohmic-resistance breakdown performed with the model showed that the high-frequency resistance contains membrane resistance and electronic resistance of other components, but does not include protonic resistance of the carbon-supported catalyst layers and thus is not equivalent to the total

ohmic resistance of the cell.

Conflicts of interest

There are no conflicts to declare.

Acknowledgement

The authors thank Dr. Petar Minev (Department of Mathematical and Statistical Sciences, University of Alberta) for the scientific guidance during the development of the transient framework in OpenFCST, Fei Wei and Manas Mandal (Energy Systems Design Laboratory, Department of Mechanical Engineering, University of Alberta) for providing the mercury-intrusion porosimetry data of the micro-porous layers and SEM images of the catalyst layers, respectively, and Dr. Jonathan Sharman (Johnson Matthey, UK) for the fruitful discussions of this work. The authors also acknowledge the Natural Sciences and Engineering Council of Canada (NSERC), CREATE-ME^2 (Collaborative Research and Training Experience Program - Materials for Electrochemical Energy Solutions Initiative), the Automotive Fuel Cell Cooperation Corporation (AFCC), and Johnson Matthey for their financial assistance.

References

[1] U.S. Department of Energy, Fuel cell technologies office multi-year research, development, and demonstration plan: Fuel cells, `https://energy.gov/sites/prod/files/2017/05/f34/fcto_myrdd_fuel_cells.pdf`, accessed on November 10, 2019. (2017).

[2] D. Papageorgopoulos, Fuel cell R&D overview, `https://www.hydrogen.energy.gov/pdfs/review19/plenary_fuel_cell_papageorgopoulos_2019.pdf`, accessed on November 10, 2019 (2019).

[3] A. Kongkanand, M. F. Mathias, The priority and challenge of high-power performance of low-platinum proton-exchange membrane fuel cells, The journal of physical chemistry letters 7 (7) (2016) 1127–1137 (2016).

[4] H. Iden, K. Sato, A. Ohma, K. Shinohara, Relationship among microstructure, ionomer property and proton transport in pseudo catalyst layers, Journal of The Electrochemical Society 158 (8) (2011) B987–B994 (2011).

[5] C. K. Mittelsteadt, H. Liu, Conductivity, permeability, and ohmic shorting of ionomeric membranes, in: W. Vielstich, H. A. Gasteiger, H. Yokokawa (Eds.), Handbook of fuel cells: Fundamentals technology and applications: Advances in electrocatalysis, materials, diagnostics and durability, Springer New York, John Wiley & Sons, 2009, pp. 345–358 (2009).

[6] J. Peron, A. Mani, X. Zhao, D. Edwards, M. Adachi, T. Soboleva, Z. Shi, Z. Xie, T. Navessin, S. Holdcroft, Properties of Nafion® NR-211 membranes for PEMFCs, Journal of Membrane Science 356 (1-2) (2010) 44–51 (2010).

[7] W. He, G. Lin, T. Van Nguyen, Diagnostic tool to detect electrode flooding in proton-exchange-membrane fuel cells, AIChE Journal 49 (12) (2003) 3221–3228 (2003).

[8] C. Ziegler, H. M. Yu, J. O. Schumacher, Two-phase dynamic modeling of PEMFCs and simulation of cyclovoltammograms, Journal of The Electrochemical Society 152 (8) (2005) A1555–A1567 (2005).

[9] H. Yu, C. Ziegler, Transient behavior of a proton exchange membrane fuel cell under dry operation, Journal of The Electrochemical Society 153 (3) (2006) A570–A575 (2006).

[10] L. Hao, H. Yu, J. Hou, W. Song, Z. Shao, B. Yi, Transient behavior of water generation in a proton exchange membrane fuel cell, Journal of Power Sources 177 (2) (2008) 404–411 (2008).

[11] D. Gerteisen, T. Heilmann, C. Ziegler, Modeling the phenomena of dehydration and flooding of a polymer electrolyte membrane fuel cell, Journal of Power Sources 187 (1) (2009) 165–181 (2009).

[12] J. Hou, A study on polarization hysteresis in PEM fuel cells by galvanostatic step sweep, International Journal of Hydrogen Energy 36 (12) (2011) 7199–7206 (2011).

[13] A. Goshtasbi, P. García-Salaberri, J. Chen, K. Talukdar, D. G. Sanchez, T. Ersal, Through-the-membrane transient phenomena in PEM fuel cells: A modeling study, Journal of The Electrochemical Society 166 (7) (2019) F3154–F3179 (2019).

[14] D. Malevich, E. Halliop, B. A. Peppley, J. G. Pharoah, K. Karan, Investigation of charge-transfer and mass-transport resistances in PEMFCs with microporous layer using electrochemical impedance spectroscopy, Journal of The Electrochemical Society 156 (2) (2009) B216–B224 (2009).

[15] D. Malevich, B. R. Jayasankar, E. Halliop, J. G. Pharoah, B. A. Peppley, K. Karan, On the determination of PEM fuel cell catalyst layer resistance from impedance measurement in H2/N2 cells, Journal of the Electrochemical Society 159 (12) (2012) F888–F895 (2012).

[16] M. Cimenti, D. Bessarabov, M. Tam, J. Stumper, Investigation of proton transport in the catalyst layer of PEM fuel cells by electrochemical impedance spectroscopy, ECS transactions 28 (23) (2010) 147–157 (2010).

[17] R. Makharia, M. Mathias, D. Baker, Measurement of catalyst layer electrolyte resistance in PEFCs using electrochemical impedance spectroscopy, Journal of The Electrochemical Society 152 (5) (2005) A970–A977 (2005).

[18] I. Pivac, F. Barbir, Inductive phenomena at low frequencies in impedance spectra of proton exchange membrane fuel cells–A review, Journal of Power Sources 326 (2016) 112–119 (2016).

[19] S. M. R. Niya, M. Hoorfar, Study of proton exchange membrane fuel cells using electrochemical impedance spectroscopy technique–A review, Journal of Power Sources 240 (2013) 281–293 (2013).

[20] A. Schiefer, M. Heinzmann, A. Weber, E. Ivers-Tiffée, Inductive low-frequency processes in PEMFC impedance spectra, in: H. Gasteiger, A. Bandarenka (Eds.), EFCF 2019: Low-Temperature Fuel Cells, Electrolisers, & H_2 Processing, Chapter 03, 2019, pp. 179–189 (2019).

[21] X.-Z. Yuan, C. Song, H. Wang, J. Zhang, Electrochemical impedance spectroscopy in PEM fuel cells: fundamentals and applications, Springer Science & Business Media, 2009 (2009).

[22] N. Zamel, A. Bhattarai, D. Gerteisen, Measurement of spatially resolved impedance spectroscopy with local perturbation, Fuel Cells 13 (5) (2013) 910–916 (2013).

[23] I. Raistrick, Impedance studies of porous electrodes, Electrochimica Acta 35 (10) (1990) 1579–1586 (1990).

[24] T. Springer, T. Zawodzinski, M. Wilson, S. Gottesfeld, Characterization of polymer electrolyte fuel cells using AC impedance spectroscopy, Journal of the Electrochemical Society 143 (2) (1996) 587–599 (1996).

[25] T. Gaumont, G. Maranzana, O. Lottin, J. Dillet, S. Didierjean, J. Pauchet, L. Guétaz, Measurement of protonic resistance of catalyst layers as a tool for degradation monitoring, International Journal of Hydrogen Energy 42 (3) (2017) 1800–1812 (2017).

[26] J. Hou, W. Song, H. Yu, Y. Fu, L. Hao, Z. Shao, B. Yi, Ionic resistance of the catalyst layer after the PEM fuel cell suffered freeze, Journal of Power Sources 176 (1) (2008) 118–121 (2008).

[27] F. Jaouen, G. Lindbergh, K. Wiezell, Transient techniques for investigating mass-transport limitations in gas diffusion electrodes ii. experimental characterization of the PEFC cathode, Journal of The Electrochemical Society 150 (12) (2003) A1711–A1717 (2003).

[28] S. Tant, S. Rosini, P.-X. Thivel, F. Druart, A. Rakotondrainibe, T. Geneston, Y. Bultel, An algorithm for diagnosis of proton exchange membrane fuel cells by electrochemical impedance spectroscopy, Electrochimica Acta 135 (2014) 368–379 (2014).

[29] B. P. Setzler, T. F. Fuller, A physics-based impedance model of proton exchange membrane fuel cells exhibiting low-frequency inductive loops, Journal of The Electrochemical Society 162 (6) (2015) F519–F530 (2015).

[30] C. Bao, W. Bessler, Two-dimensional modeling of a polymer electrolyte membrane fuel cell with long flow channel. Part II. Physics-based electrochemical impedance analysis, Journal of Power Sources 278 (2015) 675–682 (2015).

[31] G. A. Futter, P. Gazdzicki, K. A. Friedrich, A. Latz, T. Jahnke, Physical modeling of polymer-electrolyte membrane fuel cells: Understanding water management and impedance spectra, Journal of Power Sources 391 (2018) 148–161 (2018).

[32] M. Ciureanu, R. Roberge, Electrochemical impedance study of PEM fuel cells. experimental diagnostics and modeling of air cathodes, The Journal of Physical Chemistry B 105 (17) (2001) 3531–3539 (2001).

[33] M. Heinzmann, A. Weber, E. Ivers-Tiffée, Advanced modelling of PEMFC impedance spectra, in: H. Gasteiger, A. Bandarenka (Eds.), EFCF 2019: Low-Temperature Fuel Cells, Electrolisers, & H_2 Processing, Chapter 03, 2019, pp. 232–243 (2019).

[34] M. Eikerling, A. Kornyshev, Electrochemical impedance of the cathode catalyst layer in polymer electrolyte fuel cells, Journal of Electroanalytical Chemistry 475 (2) (1999) 107–123 (1999).

[35] S. Cruz-Manzo, R. Chen, A generic electrical circuit for performance analysis of the fuel cell cathode catalyst layer through electrochemical impedance spectroscopy, Journal of Electroanalytical Chemistry 694 (2013) 45–55 (2013).

[36] A. Kulikovsky, A physical model for catalyst layer impedance, Journal of Electroanalytical Chemistry 669 (2012) 28–34 (2012).

[37] A. Kulikovsky, O. Shamardina, A model for PEM fuel cell impedance: Oxygen flow in the channel triggers spatial and frequency oscillations of the local impedance, Journal of The Electrochemical Society 162 (9) (2015) F1068–F1077 (2015).

[38] A. Baricci, M. Zago, A. Casalegno, A quasi 2D model of a high temperature polymer fuel cell for the interpretation of impedance spectra, Fuel Cells 14 (6) (2014) 926–937 (2014).

[39] C. Bao, W. Bessler, Two-dimensional modeling of a polymer electrolyte membrane fuel cell with long flow channel. Part I. Model development, Journal of Power Sources 275 (2015) 922–934 (2015).

[40] J. Vang, F. Zhou, S. Andreasen, S. Kær, Estimating important electrode parameters of high temperature PEM fuel cells by fitting a model to polarisation curves and impedance spectra, Ecs Transactions 68 (3) (2015) 13–34 (2015).

[41] M. Bhaiya, An open-source two-phase non-isothermal mathematical model of a polymer electrolyte membrane fuel cell, Master's thesis, University of Alberta (2014).

[42] M. Bhaiya, A. Putz, M. Secanell, Analysis of non-isothermal effects on polymer electrolyte fuel cell electrode assemblies, Electrochimica Acta 147 (2014) 294–309 (2014).

[43] M. Secanell, A. Putz, S. Shukla, P. Wardlaw, M. Bhaiya, L. M. Pant, M. Sabharwal, Mathematical Modelling and Experimental Analysis of Thin, Low-Loading Fuel Cell Electrodes, ECS Transactions 69 (17) (2015) 157–187 (2015).

[44] K. Cooper, M. Smith, Electrical test methods for on-line fuel cell ohmic resistance measurement, Journal of Power Sources 160 (2) (2006) 1088–1095 (2006).

[45] J. Zhou, S. Shukla, A. Putz, M. Secanell, Analysis of the role of the microporous layer in improving polymer electrolyte fuel cell performance, Electrochimica Acta 268 (2018) 366–382 (2018).

[46] T. Springer, T. Zawodzinski, S. Gottesfeld, Polymer electrolyte fuel cell model, Journal of the Electrochemical Society 138 (8) (1991) 2334–2342 (1991).

[47] M. Secanell, Computational modeling and optimization of proton exchange membrane fuel cells, Ph.D. thesis, University of Victoria (2007).

[48] M. Secanell, R. Songprakorp, A. Suleman, N. Djilali, Multi-objective optimization of a polymer electrolyte fuel cell membrane electrode assembly, Energy & Environmental Science 1 (3) (2008) 378–388 (2008).

[49] J. Zhou, A. Putz, M. Secanell, A mixed wettability pore size distribution based mathematical model for analyzing two-phase flow in porous electrodes I. Mathematical model, Journal of The Electrochemical Society 164 (6) (2017) F530–F539 (2017).

[50] J. X. Wang, F. A. Uribe, T. E. Springer, J. Zhang, R. R. Adzic, Intrinsic kinetic equation for oxygen reduction reaction in acidic media: the double Tafel slope and fuel cell applications, Faraday discussions 140 (2009) 347–362 (2009).

[51] M. Moore, A. Putz, M. Secanell, Investigation of the orr using the double-trap intrinsic kinetic model, Journal of the Electrochemical Society 160 (6) (2013) F670–F681 (2013).

[52] J. X. Wang, T. E. Springer, R. R. Adzic, Dual-pathway kinetic equation for the hydrogen oxidation reaction on Pt electrodes, Journal of the Electrochemical Society 153 (9) (2006) A1732–A1740 (2006).

[53] P. Wardlaw, Modelling of PEMFC Catalyst Layer Mass Transport and Electro-Chemical Reactions Using Multi-scale Simulations, Master's thesis, University of Alberta (2014).

[54] Lion Specialty Chemicals Co., Ltd., KETJENBLACK Highly Electro-Conductive Carbon Black (Product Information), https://www.lion-specialty-chem.co.jp/en/product/carbon/carbon01.htm, accessed on November 10, 2019.

[55] M. Secanell, A. Jarauta, A. Kosakian, M. Sabharwal, J. Zhou, PEM fuel cells, modeling, in: R. A. Meyers (Ed.), Encyclopedia of Sustainability Science and Technology, Springer New York, New York, NY, 2017, pp. 1–61 (2017). doi:10.1007/978-1-4939-2493-6_1019-1.

[56] R. B. Bird, W. E. Stewart, E. N. Lightfoot, Transport Phenomena, 2nd Edition, Wiley international, 2002 (2002).

[57] M. Sabharwal, Microstructural and performance analysis of fuel cell electrodes, Ph.D. thesis, University of Alberta (2019).

[58] M. Sabharwal, L. M. Pant, N. Patel, M. Secanell, Computational analysis of gas transport in fuel cell catalyst layer under dry and partially saturated conditions, Journal of The Electrochemical Society 166 (7) (2019) F3065–F3080 (2019).

[59] S. Ge, X. Li, B. Yi, I.-M. Hsing, Absorption, desorption, and transport of water in polymer electrolyte membranes for fuel cells, Journal of the Electrochemical Society 152 (6) (2005) A1149–A1157 (2005).

[60] A. Z. Weber, J. Newman, Transport in polymer-electrolyte membranes II. Mathematical model, Journal of The Electrochemical Society 151 (2) (2004) A311–A325 (2004).

[61] S. Kim, M. Mench, Investigation of temperature-driven water transport in polymer electrolyte fuel cell: Thermo-osmosis in membranes, Journal of Membrane Science 328 (1-2) (2009) 113–120 (2009).

[62] K. P. Domican, Mathematical modeling and experimental validation of thin low platinum content and functionally graded cathode catalyst layers, Master's thesis, University of Alberta (2014).

[63] M. Khandelwal, M. Mench, Direct measurement of through-plane thermal conductivity and contact resistance in fuel cell materials, Journal of Power Sources 161 (2) (2006) 1106–1115 (2006).

[64] O. S. Burheim, H. Su, H. H. Hauge, S. Pasupathi, B. G. Pollet, Study of thermal conductivity of pem fuel cell catalyst layers, international journal of hydrogen energy 39 (17) (2014) 9397–9408 (2014).

[65] S. Motupally, A. J. Becker, J. W. Weidner, Diffusion of water in Nafion 115 membranes, Journal of The Electrochemical Society 147 (9) (2000) 3171–3177 (2000).

[66] P. Dobson, Investigation of the polymer electrolyte membrane fuel cell catalyst layer microstructure, Master's thesis, University of Alberta (2011).

[67] P. Dobson, C. Lei, T. Navessin, M. Secanell, Characterization of the PEM fuel cell catalyst layer microstructure by nonlinear least-squares parameter estimation, Journal of the Electrochemical Society 159 (5) (2012) B514–B523 (2012).

[68] O. Burheim, P. Vie, J. Pharoah, S. Kjelstrup, Ex situ measurements of through-plane thermal conductivities in a polymer electrolyte fuel cell, Journal of Power Sources 195 (1) (2010) 249–256 (2010).

[69] R. Schweiss, C. Meiser, T. Damjanovic, I. Galbiati, N. Haak, SIGRACET gas diffusion layers for PEM fuel cells, electrolyzers and batteries, White paper SGL Group (2016).

[70] S. Shukla, F. Wei, M. Mandal, J. Zhou, M. Saha, J. Stumper, M. Secanell, Determination of PEFC gas diffusion layer and catalyst layer porosity utilizing Archimedes principle, Journal of The Electrochemical Society 166 (15) (2019) F1142–F1147 (2019).

[71] H. Xu, Experimental measurement of mass transport parameters of gas diffusion layer and catalyst layer in pem fuel cell, Master's thesis, University of Alberta (2019).

[72] P. Mangal, Experimental study of mass transport parameters of PEMFC porous media, Master's thesis, University of Alberta (2014).

[73] N. Zamel, E. Litovsky, S. Shakhshir, X. Li, J. Kleiman, Measurement of in-plane thermal conductivity of carbon paper diffusion media in the temperature range of -20 °C to +120 °C, Applied energy 88 (9) (2011) 3042–3050 (2011).

[74] N. Zamel, E. Litovsky, X. Li, J. Kleiman, Measurement of the through-plane thermal conductivity of carbon paper diffusion media for the temperature range from -50 to +120 °C, international journal of hydrogen energy 36 (19) (2011) 12618–12625 (2011).

[75] O. S. Burheim, G. A. Crymble, R. Bock, N. Hussain, S. Pasupathi, A. du Plessis, S. le Roux, F. Seland, H. Su, B. G. Pollet, Thermal conductivity in the three layered regions of micro porous layer coated porous transport layers for the pem fuel cell, international journal of hydrogen energy 40 (46) (2015) 16775–16785 (2015).

[76] R. Bock, A. Shum, T. Khoza, F. Seland, N. Hussain, I. V. Zenyuk, O. S. Burheim, Experimental study of thermal conductivity and compression measurements of the gdl-mpl interfacial composite region, ECS Transactions 75 (14) (2016) 189–199 (2016).

[77] N. Zamel, J. Becker, A. Wiegmann, Estimating the thermal conductivity and diffusion coefficient of the microporous layer of polymer electrolyte membrane fuel cells, Journal of Power Sources 207 (2012) 70–80 (2012).

[78] A. Vorobev, O. Zikanov, T. Shamim, A computational model of a PEM fuel cell with finite vapor absorption rate, Journal of Power Sources 166 (1) (2007) 92–103 (2007).

[79] A. Shah, G.-S. Kim, P. Sui, D. Harvey, Transient non-isothermal model of a polymer electrolyte fuel cell, Journal of Power Sources 163 (2) (2007) 793–806 (2007). doi:10.1016/j.jpowsour.2006.09.022.

[80] A. Roy, M. Serincan, U. Pasaogullari, M. Renfro, B. Cetegen, Transient computational analysis of proton exchange membrane fuel cells during load change and non-isothermal start-up, in: ASME 2009 7th International Conference on Fuel Cell Science, Engineering and Technology, American Society of Mechanical Engineers, 2009, pp. 429–438 (2009).

[81] A. Verma, R. Pitchumani, Influence of membrane properties on the transient behavior of polymer electrolyte fuel cells, Journal of Power Sources 268 (2014) 733–743 (2014).

[82] G. Zhang, L. Fan, J. Sun, K. Jiao, A 3D model of PEMFC considering detailed multiphase flow and anisotropic transport properties, International Journal of Heat and Mass Transfer 115 (2017) 714–724 (2017).

[83] Z. Zhan, H. Zhao, P. C. Sui, P. Jiang, M. Pan, N. Djilali, Numerical analysis of ice-induced stresses in the membrane electrode assembly of a PEM fuel cell under sub-freezing operating conditions, International Journal of Hydrogen Energy 43 (9) (2018) 4563–4582 (2018).

[84] S. Li, J. Yuan, G. Xie, B. Sundén, Effects of agglomerate model parameters on transport characterization and performance of PEM fuel cells, International Journal of Hydrogen Energy 43 (17) (2018) 8451–8463 (2018).

[85] A. Kusoglu, A. Kwong, K. T. Clark, H. P. Gunterman, A. Z. Weber, Water uptake of fuel-cell catalyst layers, Journal of The Electrochemical Society 159 (9) (2012) F530–F535 (2012).

[86] G. C. Abuin, M. C. Fuertes, H. R. Corti, Substrate effect on the swelling and water sorption of Nafion nanomembranes, Journal of membrane science 428 (2013) 507–515 (2013).

[87] A. Kusoglu, D. Kushner, D. K. Paul, K. Karan, M. A. Hickner, A. Z. Weber, Impact of substrate and processing on confinement of Nafion thin films, Advanced Functional Materials 24 (30) (2014) 4763–4774 (2014).

[88] U. N. Shrivastava, H. Fritzsche, K. Karan, Interfacial and bulk water in ultrathin films of Nafion, 3M PFSA, and 3M PFIA ionomers on a polycrystalline platinum surface, Macromolecules 51 (23) (2018) 9839–9849 (2018).

[89] C.-Y. Jung, S.-C. Yi, Influence of the water uptake in the catalyst layer for the proton exchange membrane fuel cells, Electrochemistry Communications 35 (2013) 34–37 (2013).

[90] H. K. Shim, Water sorption properties of sub-micron thin ionomer films, Master's thesis, Queen's University (2016).

[91] H. K. Shim, D. K. Paul, K. Karan, Resolving the contradiction between anomalously high water uptake and low conductivity of nanothin Nafion films on SiO2 substrate, Macromolecules 48 (22) (2015) 8394–8397 (2015).

[92] P. Krtil, A. Trojánek, Z. Samec, Kinetics of water sorption in Nafion thin films: Quartz crystal microbalance study, The Journal of Physical Chemistry B 105 (33) (2001) 7979–7983 (2001).

[93] A. Kongkanand, Interfacial water transport measurements in Nafion thin films using a quartz-crystal microbalance, The Journal of Physical Chemistry C 115 (22) (2011) 11318–11325 (2011).

[94] T. A. Zawodzinski Jr, M. Neeman, L. O. Sillerud, S. Gottesfeld, Determination of water diffusion coefficients in perfluorosulfonate ionomeric membranes, The Journal of Physical Chemistry 95 (15) (1991) 6040–6044 (1991).

[95] A. Kusoglu, A. Z. Weber, New insights into perfluorinated sulfonic-acid ionomers, Chemical reviews 117 (3) (2017) 987–1104 (2017).

[96] S. Shukla, D. Stanier, M. Saha, J. Stumper, M. Secanell, Analysis of inkjet printed PEFC electrodes with varying platinum loading, Journal of The Electrochemical Society 163 (7) (2016) F677–F687 (2016).

[97] M. Secanell, A. Putz, P. Wardlaw, V. Zingan, M. Bhaiya, M. Moore, J. Zhou, C. Balen, K. Domican, Openfcst: An open-source mathematical modelling software for polymer electrolyte fuel cells, ECS Transactions 64 (3) (2014) 655–680 (2014).

[98] OpenFCST: Open-Source Fuel Cell Simulation Toolbox (official website), `www.openfcst.org`, accessed on November 10, 2019.

[99] I. Faragó, Á. Havasi, Z. Zlatev, Efficient implementation of stable richardson extrapolation algorithms, Computers & Mathematics with Applications 60 (8) (2010) 2309–2325 (2010).

[100] E. Hairer, S. P. Nørsett, G. Wanner, Solving Ordinary Differential Equations I: Nonstiff Problems, Springer Series in Computational Mathematics, Springer, 1993 (1993).

[101] W. G. Bessler, Rapid impedance modeling via potential step and current relaxation simulations, Journal of The Electrochemical Society 154 (11) (2007) B1186–B1191 (2007).

[102] H. Wiese, K. G. Weil, An efficient fourier transform algorithm for frequency domains of several decades using logarithmically spaced time samples, IEEE Transactions on Acoustics, Speech, and Signal Processing 36 (7) (1988) 1096–1099 (1988).

[103] S. Shukla, K. Domican, K. Karan, S. Bhattacharjee, M. Secanell, Analysis of low platinum loading thin polymer electrolyte fuel cell electrodes prepared by inkjet printing, Electrochimica Acta 156 (2015) 289–300 (2015).

[104] M. Mandal, A. Valls, N. Gangnus, M. Secanell, Analysis of inkjet printed catalyst coated membranes for polymer electrolyte electrolyzers, Journal of The Electrochemical Society 165 (7) (2018) F543–F552 (2018).

[105] K. Cooper, In situ PEM fuel cell electrochemical surface area & catalyst utilization measurement, Fuel cell (2009).

[106] M. E. Orazem, B. Tribollet, Electrochemical impedance spectroscopy, 2nd Edition, John Wiley & Sons, 2017 (2017).

[107] M. Schönleber, D. Klotz, E. Ivers-Tiffée, A method for improving the robustness of linear kramers-kronig validity tests, Electrochimica Acta 131 (2014) 20–27 (2014).

[108] A. Verma, R. Pitchumani, Analysis and optimization of transient response of polymer electrolyte fuel cells, Journal of Fuel Cell Science and Technology 12 (1) (2015) 011005 (2015).

[109] O. Shamardina, M. Kondratenko, A. Chertovich, A. Kulikovsky, A simple transient model for a high temperature PEM fuel cell impedance, international journal of hydrogen energy 39 (5) (2014) 2224–2235 (2014).

[110] A. Kulikovsky, J. Divisek, A. Kornyshev, Modeling the cathode compartment of polymer electrolyte fuel cells: dead and active reaction zones, Journal of the Electrochemical Society 146 (11) (1999) 3981–3991 (1999).

[111] I. Zenyuk, P. Das, A. Weber, Understanding impacts of catalyst-layer thickness on fuel-cell performance via mathematical modeling, Journal of The Electrochemical Society 163 (7) (2016) F691–F703 (2016).

[112] R. J. Balliet, J. Newman, Cold start of a polymer-electrolyte fuel cell I. Development of a two-dimensional model, Journal of the Electrochemical Society 158 (8) (2011) B927–B938 (2011).

[113] C. A. Balen, A multi-component mass transport model for polymer electrolyte fuel cells, Master's thesis, University of Alberta (2016).

[114] J. Zhou, D. Stanier, A. Putz, M. Secanell, A mixed wettability pore size distribution based mathematical model for analyzing two-phase flow in porous electrodes II. Model validation and analysis of micro-structural parameters, Journal of The Electrochemical Society 164 (6) (2017) F540–F556 (2017).

[115] A. Parthasarathy, S. Srinivasan, A. J. Appleby, C. R. Martin, Pressure dependence of the oxygen reduction reaction at the platinum microelectrode/Nafion interface: Electrode kinetics and mass transport, Journal of the Electrochemical Society 139 (10) (1992) 2856–2862 (1992).

[116] B. Jayasankar, K. Karan, O2 electrochemistry on Pt: A unified multi-step model for oxygen reduction and oxide growth, Electrochimica Acta 273 (2018) 367–378 (2018).

[117] D. Novitski, S. Holdcroft, Determination of O_2 mass transport at the Pt|PFSA ionomer interface under reduced relative humidity, ACS Applied Materials & Interfaces 7 (49) (2015) 27314–27323 (2015).

[118] D. Novitski, A. Kosakian, T. Weissbach, M. Secanell, S. Holdcroft, Electrochemical reduction of dissolved oxygen in alkaline, solid polymer electrolyte films, Journal of the American Chemical Society 138 (47) (2016) 15465–15472 (2016).

[119] G. Maranzana, J. Mainka, O. Lottin, J. Dillet, A. Lamibrac, A. Thomas, S. Didierjean, A proton exchange membrane fuel cell impedance model taking into account convection along the air channel: On the bias between the low frequency limit of the impedance and the slope of the polarization curve, Electrochimica Acta 83 (2012) 13–27 (2012).

[120] A. Kulikovsky, A model for local impedance of the cathode side of pem fuel cell with segmented electrodes, Journal of the Electrochemical Society 159 (7) (2012) F294–F300 (2012).